Research article

# A petrological, geochemical, and geochronological study of Ramlat Fasad 532: An Omani addition to the Antarctic 'YAMM' lunar meteorite group

Bre H. Oliveira[1✉]◉   Joshua F. Snape[1]◉   Romain Tartèse[1]◉   Heejin Jeon[2]◉
Martin J. Whitehouse[2]◉   Katherine H. Joy[1]◉

[1]  Department of Earth and Environmental Sciences, The University of Manchester, Manchester, UK
[2]  Department of Geosciences, The Swedish Museum of Natural History, Stockholm, Sweden

✉ **Correspondence to:** B. H. Oliveira: breanna.tilley@manchester.ac.uk

**Author contributions:** Conceptualization: BHO, JFS, KHJ; Data curation: BHO; Formal analysis: BHO, JFS; Funding acquisition: JFS, RT, KHJ; Investigation: BHO, JFS, RT, HJ, MJW; Resources: HJ, MJW; Supervision: JFS, RT, KHJ; Visualization: BHO; Writing – original draft: BHO; Writing – review & editing: JFS, RT, KHJ.

**Data, code, and outputs:** https://doi.org/10.48420/28902935.v1

Ramlat Fasad (RF) 532 is a lunar meteorite recovered from the desert plains of Oman in 2018 during systematic searching. Our study shows that RF 532 is a monomict gabbro breccia, dominantly composed of anorthitic plagioclase and augitic to pigeonitic pyroxene. *In situ* Pb isotope analyses of feldspars, pyroxene, symplectite, apatite, zircon, and zirconolite reveal a minimum crystallisation age of 3858.9 ± 3.2 Ma (2σ uncertainty), and Pb isotope evolution modelling indicates that it was derived from a source with a $^{238}U/^{204}Pb$ ratio of ∼71–81 (typically referred to as the μ-value). With a monomict brecciated texture, partly maskelynitised plagioclase, and melt pockets and veins, it was likely subject to shock pressures of ∼20–25 GPa. In terms of petrology, geochemistry, and geochronology, RF 532 is indistinguishable from the 'YAMM' meteorites—Yamato 793169, Asuka 881757, Miller Range 05035, and Meteorite Hills 01210, which are basaltic/gabbroic lunar meteorites recovered from various Antarctic icefields—indicating that all the stones are grouped. Together, they sample a basaltic lava flow and overlying regolith that has been subject to at least one impact event. They were likely ejected from the Moon at the same time, but differences in terrestrial residence ages and recovery locations suggest they did not fall to Earth in the same event. Thus, RF 532 and the YAMM group become the first lunar launch group where all members were recovered during systematic searches, with precise recovery coordinates for all meteorites.

## 1   Introduction

As of April, 2025, over 730 lunar meteorites have been recognised and classified in the Meteoritical Bulletin (https://www.lpi.usra.edu/meteor/), of which ∼60 % of the stones are paired or grouped, such as the Dhofar (Dho) 303 clan or the Northwest Africa (NWA) 7611 clan (Korotev and Irving, 2021). Lunar meteorites may be *launch paired* (also referred to as source-crater paired) or *fall paired* (also referred to as terrestrially paired). Launch pairing occurs when a single impactor generates multiple meteoroids that end up on Earth, whereas fall pairing occurs when a single meteoroid fragments during transit and several stones land on Earth (Fritz, 2012; Korotev and Irving, 2021). In the case of fall pairing, meteorites can be paired on the basis of relatively

minimal evidence—for the most part, a close proximity in their find locations and similarities in petrography and geochemical composition is enough. For example, LaPaz Icefield (LAP) 02205, 02224, 02226, 02436, 03632, and 04841 are a group of basaltic lunar meteorites that were found along a linear trend of a few kilometres within the same Antarctic icefield (Righter et al., 2005; Zeigler et al., 2005; Day et al., 2006b; Joy et al., 2006; Hill et al., 2009). For launch pairs, similarities in petrography and geochemical compositions alone are not enough to definitively confirm pairing, and, thus, more thorough analyses are required. This can be done through a number of means, like deriving the minimum crystallisation ages for igneous samples (e.g., when a basaltic lava flow cooled on the Moon; Wang et al.,

2012; Elardo et al., 2014; Merle et al., 2024), cosmic ray exposure (CRE) ages for breccia samples (the duration a meteoroid/meteorite has been exposed to cosmic rays, e.g., Nishiizumi et al., 1992; can also be used to disprove pairing, e.g., Mészáros et al., 2017), or terrestrial residence ages (the duration a meteorite has resided on the Earth's surface; e.g., Welten et al., 2006).

In this study, we investigate Ramlat Fasad (RF) 532, which is a lunar meteorite that was recovered from the desert plains of Zufar, Oman, in 2018 during a systematic search for meteorites. It was found as a single stone weighing 245.2 g that was strongly wind-ablated and missing a fusion crust (Gattacceca et al., 2022). A likely paired stone, RF 535, is a lunar gabbro exhibiting a brecciated texture and was found as a single 116.2 g fragment only 118 m away (Gattacceca et al., 2025).

Initial classification (see Gattacceca et al., 2022) identified RF 532 as a gabbro exhibiting a brecciated texture, where large coarse-grained clasts composed of plagioclase and pyroxene are set in a matrix of fragmented minerals with the same composition. The petrography and composition of RF 532 are remarkably similar to samples in the lunar meteorite 'YAMM' group—consisting of Yamato (Y-)793169, Asuka (A-)881757, Miller Range (MIL) 05035, and the Meteorite Hills (MET) 01210 basaltic clasts (Yanai, 1991; Yanai and Kojima, 1991; Jolliff et al., 1993; Koeberl et al., 1993; Takeda et al., 1993; Joy et al., 2008; Arai et al., 2010)—suggesting grouping relations between them. However, the YAMM stones were recovered from various icefields in Antarctica (Yanai, 1991; Yanai and Kojima, 1991; Russell et al., 2004; Connolly et al., 2007), while RF 532 was recovered from Oman (Gattacceca et al., 2022). The YAMM meteorites have low bulk rock $TiO_2$ and very low incompatible trace element concentrations. Their chemical signatures are consistent with an origin from a depleted mantle source, making them useful samples for investigating the nature of depleted lunar reservoirs and the evolution of the lunar magma ocean (e.g., Misawa et al., 1993; Torigoye-Kita et al., 1995; Merle et al., 2024).

By conducting a thorough analysis of RF 532, including a comprehensive study of its petrology, geochemistry, and geochronology, we assess whether it is grouped with the YAMM stones and the potential implications for the Moon-to-Earth lunar meteorite delivery system.

## 2 Analytical methods

We mounted a 423.6 mg piece of RF 532 in a ∼2.54 cm circular epoxy puck using Buehler EpoxiCure 2 resin and polished it to a <1 μm finish using a combination of Buehler CarbiMet SiC abrasive paper, Kempad-Pan polishing cloth, and KEMET Diamond Compound.

### 2.1 Petrography, mineralogy, and major and minor element mineral chemistry

We collected full section back-scattered electron (BSE) and energy dispersive spectroscopy (EDS) X-ray element maps, along with high-resolution BSE images and targeted EDS spectra for areas of interest using scanning electron microscopy (SEM). This work was carried out at the University of Manchester (UoM) with a Hitachi TM4000Plus tabletop microscope and Aztec software (version 6.1) for data processing. We operated the instrument in high-vacuum mode, using an accelerating voltage of 20 kV, a current of 2 nA, and a working distance of 10 mm.

We collected major and minor element mineral chemistry (i.e., Ba, Ca, Cr, Fe, K, Mg, Mn, Na, Ni, P, Si, and Ti) on silicates and glasses using electron probe microanalysis (EPMA). This work was carried out at the UoM with a Cameca SX 100 equipped with a BSE detector and five wavelength dispersive spectrometers. For pyroxene and olivine, we used an accelerating voltage of 15 kV, beam current of 10 nA, and beam size of 2 μm. For plagioclase and K-feldspar, we used an accelerating voltage of 15 kV, beam current of 5 nA, and beam size of 5 μm. For glasses, we used an accelerating voltage of 15 kV, beam current of 2 nA, and beam size of 10 μm. The instrument was calibrated using a suite of UoM standards, as well as National Museum of Natural History (NMNH) 137041 anorthite (Jarosewich et al., 1980a,b). We used NMNH 122142 Kakanui augite, NMNH 111312-44 San Carlos olivine, and NMNH 137041 anorthite as secondary standards for our silicate analyses, and the United States Geological Survey (USGS) glasses BIR-2G and BHVO-2G as secondary standards for our glass analyses. During analysis, we measured Na first to avoid volatilisation. The interferences of Ba on Ti (and vice versa) were accounted for using NMNH 86539 benitoite and an in-house Ba glass standard. Data were reviewed to ensure measured concentrations were above instrumental detection limits, analytical totals were within acceptable parameters (i.e., 100 ± 2.5 wt%), and relative element abundances were consistent with mineral stoichiometry. The full suite of standards and data are available in Oliveira et al. (2025), Tables S1.1 and S1.2.

### 2.2 Trace element mineral chemistry

We carried out trace element analyses on silicates and glasses using laser ablation inductively coupled mass spectrometry (LA-ICP-MS). This work was carried out at the UoM using a Teledyne Photon Machines Analyte Excite+ 193 nm ArF excimer laser ablation system with a HelEx II active 2-volume ablation cell coupled to an Agilent 8900 ICP-MS via a signal-smoothing device. Plagioclase, pyroxene, and glass were analysed using a 65 μm circular spot size, a fluence of $4 \, J \, cm^{-2}$, and a repetition rate of 5 Hz. Each analysis lasted 40 s duration and was preceded by 20 s of integration of the gas blank to assess background levels. Ablated material was carried to the ICP-MS via high purity He that was mixed with Ar prior to injection in the plasma source. We used the National Institute of Standards and Technology (NIST) 612 standard reference material to perform tuning and mass calibration of the ICP-MS at the start of the analytical session, optimising the ICP-MS sensitivity whilst ensuring that oxide formation remained low ($^{232}Th^{16}O^+/^{232}Th^+ < 0.20\%$) and our $^{238}U^+/^{232}Th^+$ ratio was close to unity. We reduced the data using the trace

elements data reduction scheme in Iolite (version 4, Paton et al., 2011). Trace element chemistry was internally standardised using known Ca abundances for reference materials and those measured by EPMA for RF 532 silicate and glass analyses (Oliveira et al., 2025, Table S1.2). We bracketed our unknowns every ∼10 measurements with analyses of the USGS basaltic glasses BCR-2G, BHVO-2, and BIR-1G. We used BCR-2G as our primary reference material, and BHVO-2 and BIR-1G as quality control reference materials. Our accuracy for most trace elements was typically within ± 5 % of recommended values. A summary of the analytical protocol and the full suite of trace element data are available in Oliveira et al. (2025), Tables S2.1 and S2.2, respectively.

## 2.3 Radiometric dating

We used secondary ion mass spectrometry (SIMS) for measuring Pb isotopes in multiple phases within the section, as well as for acquiring U-Th-Pb isotope systematics for apatite grains. These measurements were performed using a Cameca IMS 1280 ion microprobe at the NordSIMS facility, Swedish Museum of Natural History. The methodologies closely followed those of previous studies (e.g., Snape et al., 2016; Thiessen et al., 2017, 2018; Nemchin et al., 2021).

Prior to analysis, the sample was cleaned and a new carbon coat was applied. During the analytical session, we generated the primary oxygen beam ($O_2^-$) with an Oregon Physics Hyperion H201 radio-frequency plasma source operated in critical focusing mode and adjusted the field apertures in the secondary ion path to restrict the signal to suitable sizes for each phase. For apatite, K-feldspar, and K-rich glass phases <30 μm in size we used a primary beam current of 4 nA with a ∼10 μm raster, and for plagioclase, pyroxene, and symplectite phases >30 μm in size we used a primary beam current of either 20 or 34 nA with a ∼20 to 40 μm raster, depending on the size of the individual grain. At the start of each measurement, an area of 20–30 μm$^2$ was rastered for 40–90 s (shorter pre-analysis rastering was performed when using the higher beam currents), which removed the carbon coat and minimised surface contamination.

For Pb isotope analyses in multiple phases, $^{204}Pb^+$, $^{206}Pb^+$, $^{207}Pb^+$, and $^{208}Pb^+$ were simultaneously collected on four Hamamatsu 416 low-noise ion counting electron multipliers (EM). The mass spectrometer was operated with a mass resolution of 5390 (M/ΔM), sufficient to resolve Pb from known molecular interferences. A nuclear magnetic resonance field sensor was used to regulate the magnetic field. Each measurement consisted of 60 integrations of 20 s per cycle. Background counts were measured for 2 s during each cycle by blanking the secondary beam, with <0.005 counts/second for all detectors where Pb isotopes were measured. The full background values are available in Oliveira et al. (2025), Table S3.1. In the final dataset, we checked individual analyses to ensure that the count rates for all masses were >3× the average background count rates.

Adding to the four Pb isotopes, $^{238}U^+$, $^{232}Th^{16}O^+$, $^{238}U^{16}O^+$, and $^{238}U^{16}O_2^+$ (together with the apatite/merrillite matrix peak $^{40}Ca^{31}P^{16}O_4^+$) were also measured to gain the U-Th-Pb isotope systematics for apatite. A single ETP EM was utilised to collect all species in a mass-switching sequence.

The USGS reference material BCR-2G was analysed alongside our unknowns and later used to correct for instrumental mass fractionation and detector relative gain calibration. For the gain correction, we took stated literature values ($^{206}Pb/^{204}Pb$ = 18.750, $^{207}Pb/^{204}Pb$ = 15.615, $^{208}Pb/^{204}Pb$ = 38.691; Woodhead and Hergt, 2000) and divided them by the corresponding average from the session to produce a correction factor that we then applied to our unknowns. Measurements of the USGS MPI-DING reference glass T1-G were also made throughout the session and corrected in the same manner as the unknown analyses. In all cases, the average Pb isotope ratios of the gain-corrected T1-G analyses were within 1 % of the recommended values (Jochum et al., 2011). For our U-Pb measurements, we calibrated against the ca. 2040 million-year-old BR5 apatite reference material with a $^{206}Pb/^{204}Pb$ ratio of >1000 and U concentration of 68 μg g$^{-1}$ (Kennedy et al., 2023). Our analyses of BCR-2G including gain corrections, as well as our analyses of T1-G, and our analyses of BR5 are available in Oliveira et al. (2025), Tables S3.2 and S3.3, respectively.

We processed the data using the in-house CIPS-convert SIMS data reduction spreadsheets produced by M. J. Whitehouse at NordSIMS and IsoplotR (Vermeesch, 2018), using decay constants of λ$^{238}$U = 1.55125×10$^{-10}$ year$^{-1}$ and λ$^{235}$U = 9.8485×10$^{-10}$ year$^{-1}$ (Jaffey et al., 1971; Steiger and Jäger, 1977), and a present-day $^{238}U/^{235}U$ ratio of 137.818 (Hiess et al., 2012). Our U-Pb and Pb-Pb data are available in Oliveira et al. (2025), Tables S3.4 and S3.5, respectively. All uncertainties on calculated dates are quoted to 2σ.

For our Pb-Pb isochrons, we filtered the Pb isotope data under the assumption that Pb in lunar samples is a mixture of three end-members: initial Pb, in situ radiogenic Pb, and terrestrial Pb. On a plot of $^{207}Pb/^{206}Pb$ vs. $^{204}Pb/^{206}Pb$, these end-members form a triangular field in which all data should fall. The highest $^{207}Pb/^{206}Pb$ ratios are an estimate of the initial Pb, the highest $^{204}Pb/^{206}Pb$ ratios represent terrestrial contamination, while the lowest $^{207}Pb/^{206}Pb$ and $^{204}Pb/^{206}Pb$ ratios (i.e., the y-intercept of the triangular field) indicate in situ radiogenic Pb. A two-component mixing line of initial Pb and in situ radiogenic Pb that forms the leftmost edge of the triangular field defines the isochron. In IsoplotR, we filtered out any data which fell to the right-hand side of the isochron under the assumption that they were terrestrially contaminated.

## 3 Results

### 3.1 Petrography, mineralogy, and geochemistry

Ramlat Fasad 532 is a gabbroic lunar meteorite with a brecciated texture, composed of large crystalline clasts set in a matrix made of mineral fragments (Figures 1 and 2). The clasts are coarse-grained with mineral grains measuring

anywhere from 500 to >2500 µm, and the matrix is fine- to medium-grained with grains measuring from 20–300 µm. Mineralogically, the matrix regions are composed of the same material as the clasts (Figure 2d) and interstitial melt pockets are common (Figure 2h). Large melt veins traverse the entire sample, measuring up to 760 µm in width at some sections. Throughout the melt veins themselves there are flow bands (Figure 2g), relict minerals from the host rock (Figure 2g), and 350–1500 µm diameter rounded vesicles that have been infilled with terrestrially deposited carbonates (Figure 2e-f). Cracks that have been infilled with terrestrial carbonates are pervasive throughout the sample (yellow regions in Figures 1b, 2e); it is likely that RF 532 initially had a fusion crust, but over time it was weathered away by the hot desert conditions of Oman, allowing terrestrial carbonates to penetrate into cracks in the sample.

Dominantly (>5 % of the rock), the sample itself is composed of anorthitic plagioclase that has been partly transformed to maskelynite and augitic to pigeonitic pyroxene (Figure 1). Minor phases (∼1–5 % of the rock) include fayalitic olivine, silica, ilmenite, and ulvöspinel, and accessory phases (<1 % of the rock) include K-feldspar, K-rich glass, apatite, zircon, zirconolite, and troilite. Symplectite assemblages (Figure 2b) are composed of pyroxene, olivine, and silica, and sometimes contain larger grains of the precursor mineral(s).

Plagioclase is dominantly anorthitic with a composition of $An_{90-94}$ (Figure 3). In BSE images, it appears smooth and homogenous with few cracks, suggesting at least partial transformation to maskelynite (Figure 2a,c; in line with Gattacceca et al., 2022).

Pyroxene is augitic to pigeonitic, with compositions of $En_{4-37}Fs_{32-69}Wo_{14-43}$ (Figure 4). Grains are zoned with Mg-rich cores extending to Fe-rich rims. In BSE images, grains are visibly fractured (Figure 1, Figure 2a). On a plot of Al/Ti (cations) *vs.* Fe/(Fe + Mg), pyroxene compositions show a decrease in Al/Ti when Fe/(Fe + Mg) increases from ∼0.4 to 0.6, followed by a flattening of Al/Ti at Fe/(Fe + Mg) >0.6, indicative of the co-crystallisation of ilmenite and ulvöspinel (Figure 5a). On a plot of Ti/(Ti + Cr) *vs.* Fe/(Mg + Fe), pyroxene compositions follow the aforementioned crystallisation trends and plot within the Apollo low-Ti basalt field (Figure 5b). This is in line with a reported bulk rock chemical composition of 1.95 wt% $TiO_2$ (Gattacceca et al., 2022; Paquet et al., 2025).

Some pyroxene grains have broken down to form symplectite assemblages (Figure 2b) composed of pyroxene $(En_{4-12}Fs_{51-55}Wo_{36-43})$, olivine $(Fa_{94-98})$, and silica. Some symplectite patches are fractured, suggesting that they formed prior to any major shock event(s). Across the sample, olivine is fayalitic with compositions of $Fa_{93-98}$. Ulvöspinel is homogeneous with compositions of $Chr_{1-8}Her_{2-5}Ulv_{89-95}$.

A melt vein that cuts across the sample (outlined in the lower right-hand side of Figure 1a) has an average composition of 12.3 ± 3.2 wt% $Al_2O_3$, 11.7 ± 0.6 wt% CaO, 21.6 ± 1.3 wt% FeO, 4.6 ± 2.2 wt% MgO, 44.6 ± 1.3 wt% $SiO_2$, and 2.2 ± 0.4 wt% $TiO_2$ (here, ± standard deviation, based
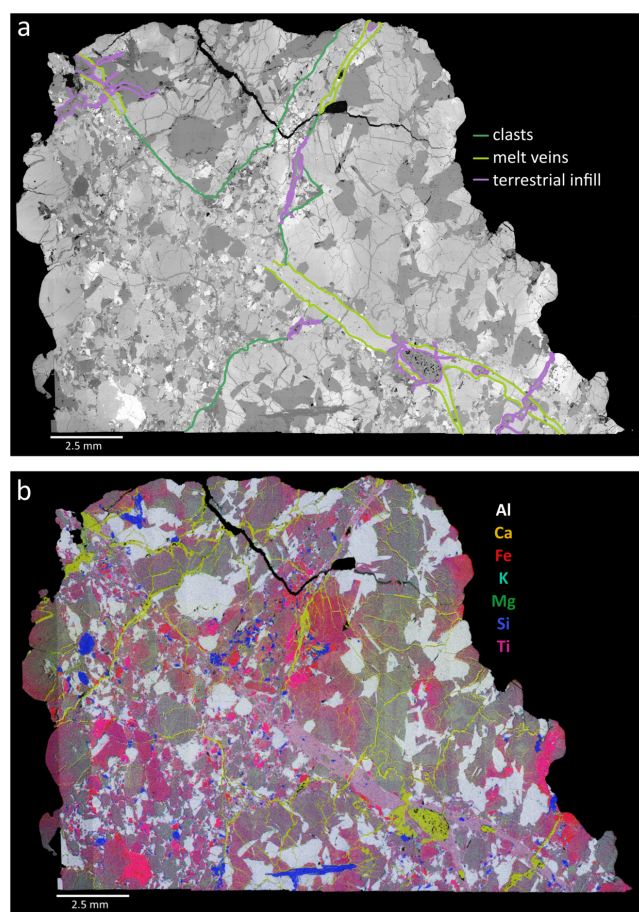
**Figure 1.** (a) SEM BSE montaged image with some major features outlined, and (b) montaged false colour X-ray map of RF 532. In (b), Al = white (plagioclase), Ca = yellow (terrestrial carbonates), Fe = red (olivine, pyroxene), K = cyan (K-feldspar, K-rich glass), Mg = green (pyroxene), Si = blue (silica), and Ti = pink (ilmenite, ulvöspinel). Close-up BSE images of features of interest are shown in Figure 2.

on 13 measurements; see Oliveira et al., 2025, Table S1.2). However, it is not homogeneous. Schlieren textures are visible in BSE images (Figure 2g) and there are geochemical variations across the melt vein as evident by the relatively large standard deviations for some oxide averages.

CI chondrite-normalised (using values from Anders and Grevesse, 1989) rare earth element (REE) patterns for plagioclase (Figure 6a) show strong positive Eu anomalies $(Eu_{CN}/Eu_{CN}* = 3.7–9.2)$ and light REE (LREE) enrichment over heavy REEs (HREE; average $La_{CN}/Lu_{CN} =$ 6.1). Chondrite-normalised REE patterns for pyroxene (Figure 6b) show negative Eu anomalies $(Eu_{CN}/Eu_{CN}* =$ 0.17–0.45) and slight HREE enrichment over LREEs (average $La_{CN}/Lu_{CN} = 0.13$). For the melt veins, chondrite-normalised REE patterns (Figure 6c) are relatively flat (average $La_{CN}/Lu_{CN} = 0.86$) with slight negative Eu anomalies $(Eu_{CN}/Eu_{CN}* = 0.31–0.47)$ and display higher REE abundances than both plagioclase and pyroxene (*ca.* 40–50 × CI values). This could be attributed to the higher abundance of small REE-rich phases present within the vein, e.g., relict apatite grains from the host rock (Figure 2g).
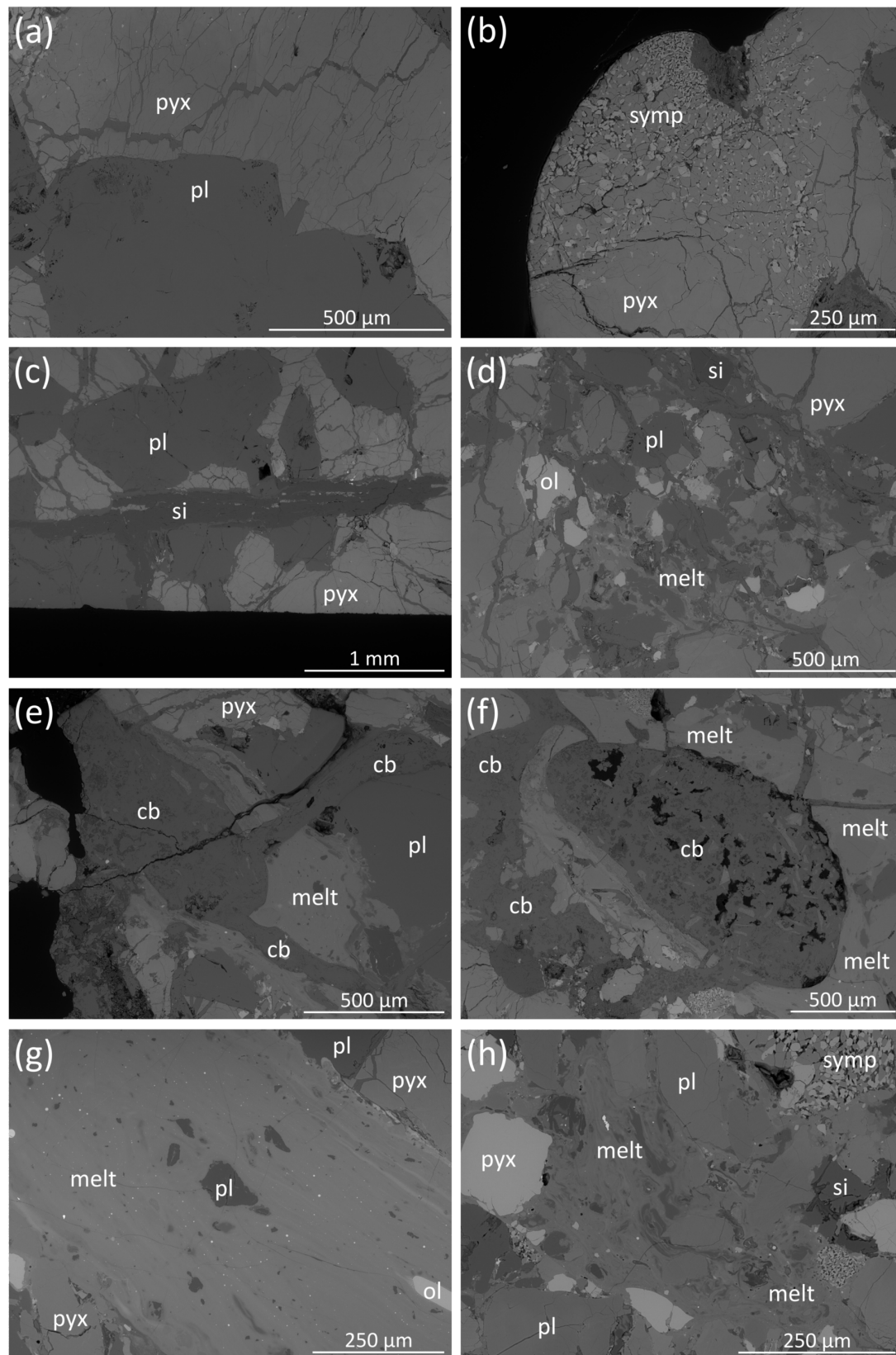
**Figure 2.** BSE images of components in RF 532. (a) Fractured pyroxene next to a plagioclase grain with a 'smooth' internal appearance, (b) breakdown of pyroxene into symplectite, (c) large lath of silica, (d) brecciated groundmass, (e-f) terrestrial carbonates hosted in fractures and vesicles within in the melt vein, (g) the melt vein with small relict mineral clasts, and (h) interstitial melt pocket located within the groundmass. Pyx = pyroxene, pl = plagioclase, symp = symplectite, si = silica, ol = olivine, and cb = terrestrial carbonates.
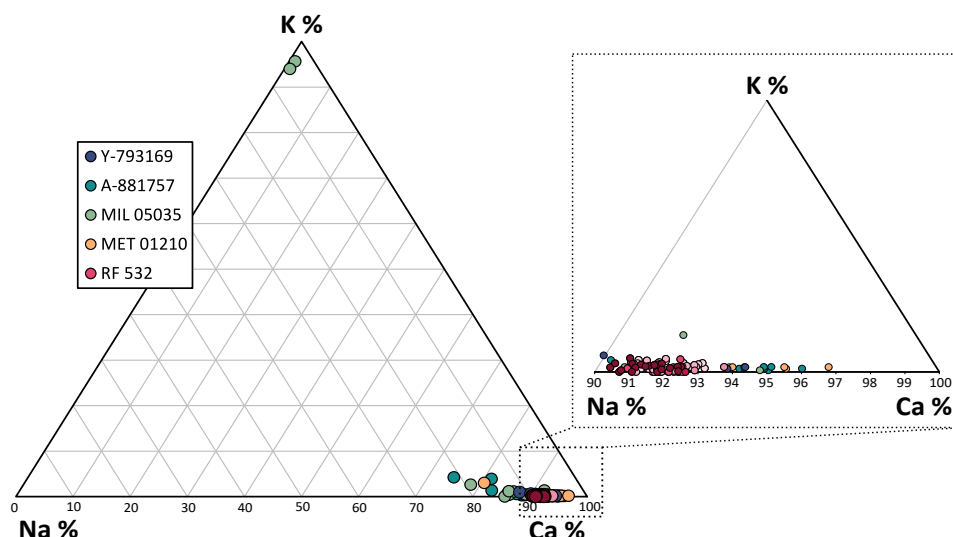
**Figure 3.** Feldspar ternary diagram illustrating the range of compositions measured in RF 532. Different shades of red-pink for RF 532 correspond to different feldspar grains. Data for the YAMM meteorites are from Jolliff et al. (1993); Koeberl et al. (1993); Takeda et al. (1993); Arai et al. (1996); Korotev et al. (2003); Day et al. (2006a); Joy et al. (2008); Liu et al. (2009); Arai et al. (2010).
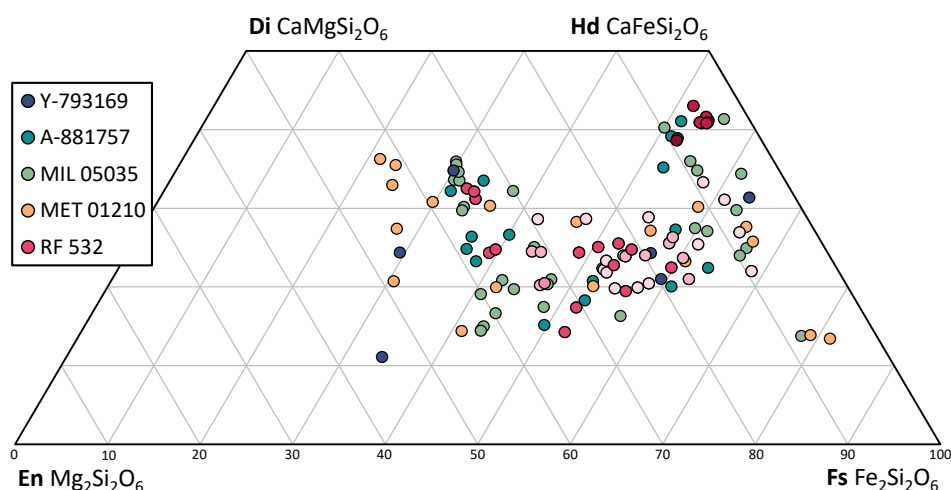


**Figure 4.** Pyroxene quadrilateral diagram illustrating the range of compositions measured in RF 532. Different shades of red-pink for RF 532 correspond to different pyroxene grains. Literature data for the YAMM meteorites are the same as those given in the Figure 3 caption.

The REE pattern for the melt vein is similar to bulk rock patterns for Y-793169 and A-881757, although with ∼2–3 times higher REE abundances in RF 532 (Figure 6c). Assuming it represents *in situ* melting of the parent lithology, it provides an estimate for the bulk rock REE contents of RF 532.

## 3.2 Geochronology

*In situ* Pb isotope analyses were carried out on one of the crystalline clasts in the sample (the large clast that covers the majority of the right half of the sample, Figure 1), targeting plagioclase, pyroxene, K-feldspar, K-rich glass, apatite, zircon, zirconolite, and symplectite. *In situ* U-Pb

dating was carried out on apatite grains throughout the sample, including grains within the crystalline clasts, the brecciated groundmass, and the melt vein. The crystalline clast yielded a Pb-Pb isochron date of 3858.9 ± 3.2 Ma (Figure 7a; n = 28 out of 51 total analyses, MSWD = 1.3, p($\chi^2$) = 0.16), with some data points filtered out due to suspected terrestrial contamination (grey data points in Figure 7a) following the approach outlined in Section 2.3. In the case of Pb isotope analyses of the melt vein (yellow data points that lie slightly above the isochron in Figure 7b), more radiogenic lunar Pb appears to have been introduced to the melt (presumably from the regolith or another lithology close to where the brecciation occurred)
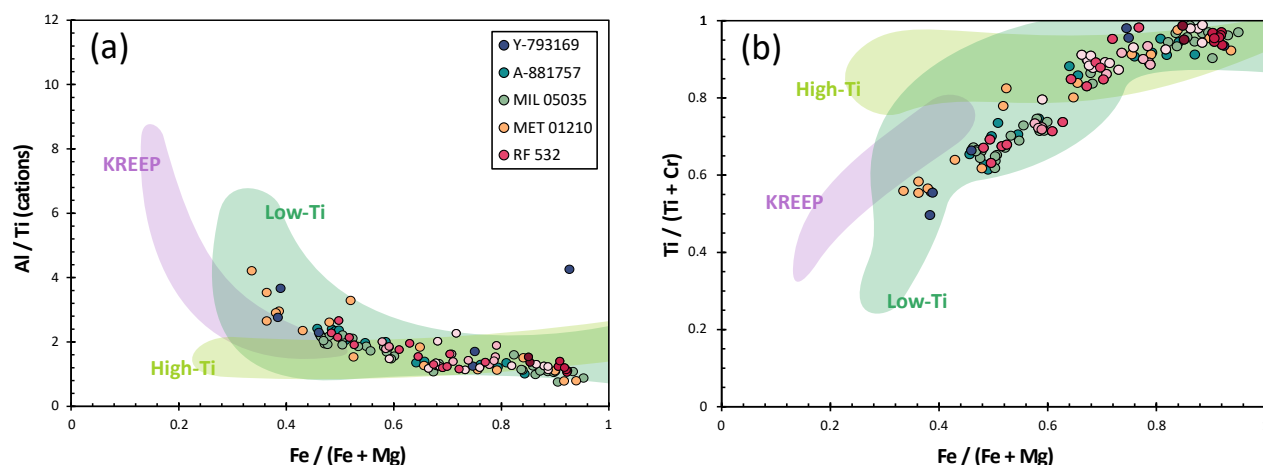
**Figure 5.** (a) Cations of Al/Ti *vs.* molar Fe/(Fe + Mg) and (b) molar Ti/(Ti + Cr) *vs.* molar Fe/(Fe + Mg), demonstrating the range of pyroxene compositions and crystallisation trends in RF 532. Different red-pink shades for RF 532 correspond to different pyroxene grains. Literature data for the YAMM meteorites are the same as those given in the Figure 3 caption, and Apollo basalt fields are based on data in Bence and Papike (1972); Dymek et al. (1975); Vaniman and Papike (1977).

and, thus, these data points have also been filtered out. Taking the weighted average of the uppermost six analyses gives a $^{207}Pb/^{206}Pb$ ratio of 1.33 ± 0.02 and corresponding $^{204}Pb/^{206}Pb$ ratio of 0.0412 ± 0.002.

Most of the apatite U-Pb analyses are from grains within the crystalline region of our sample (Figure 1). When corrected for the presence of modern terrestrial Pb, these grains have $^{207}Pb/^{206}Pb$ dates ranging from 3851 ± 37 to 3925 ± 88 Ma (Oliveira et al., 2025, Table S3.4), with a weighted mean of 3878 ± 5 Ma (n = 12 out of 12 total analyses, MSWD = 2, p($\chi^2$) = 0.023). Depending on the grain, analyses show both normal and reverse discordance (-33.6 to 24.7 %, where the reverse discordance may be due to analytical artefacts such as uneven sample surface and/or unidentified topographical variations, e.g., cracks) on a Wetherill plot and have a discordia upper intercept of 3877 ± 5.4 Ma (n = 12 out of 12 total analyses, MSWD = 2.1, p($\chi^2$) = 0.024; dark green data points in Figure 7c).

From the brecciated section, we analysed two different apatite grains. These have $^{207}Pb/^{206}Pb$ dates of 3871 ± 23 and 3880 ± 23 Ma, with a weighted mean of 3876 ± 16 Ma (n = 2 out of 2 total analyses, MSWD = 0.31, p($\chi^2$) = 0.58). Together, they plot on a concordia curve and have a concordia date of 3884 ± 15 Ma (n = 2 out of 2 total analyses, MSWD = 1.6, p($\chi^2$) = 0.21; light green data points in Figure 7c). Two analyses from an apatite grain located in the primary melt vein running through our sample have $^{207}Pb/^{206}Pb$ dates of 3867 ± 12 and 3879 ± 13 Ma, with a weighted mean of 3873 ± 9 Ma (n = 2 out of 2 total analyses, MSWD = 1.9, p($\chi^2$) = 0.17). These are reverse discordant (13.3 to 21.8 %), potentially due to analytical artefacts (e.g., uneven surface), and have a discordia upper intercept at 3872.1 ± 8.6 Ma (n = 2 out of 2 total analyses, MSWD = 1, p($\chi^2$) = 1; purple data points in Figure 7c).

Across the various lithologies in the sample apatite U-Pb systematics are consistent. Gain and terrestrial Pb corrected

$^{207}Pb/^{206}Pb$ dates range from 3857 ± 26 to 3892 ± 15 Ma, with a weighted mean of 3875.6 ± 4.4 Ma (n = 16 out of 16 total analyses, MSWD = 1.2, p($\chi^2$) = 0.23). On a concordia plot (Figure 7b), all apatite analyses are consistent with an upper intercept date of 3875.7 ± 4.5 Ma (n = 16 out of 16 total analyses, MSWD = 1.8, p($\chi^2$) = 0.035) and a lower intercept of 37 ± 101 Ma, consistent with recent Pb loss.

There is a discrepancy between the date of 3858.9 ± 3.2 Ma derived from our Pb-Pb isochron (Figure 7a) and 3875.7 ± 4.5 Ma derived from apatite U-Pb results (Figure 7c). In Figure 7b, we see that a number of analyses on apatite grains from our U-Pb session have higher $^{204}Pb/^{206}Pb$ ratios than other analyses in the sample with equivalent $^{207}Pb/^{206}Pb$ ratios, placing them to the right of the isochron. If we assume that 100 % of the non-radiogenic Pb in the grains is lunar initial (as opposed to terrestrial Pb), we can use our initial Pb composition for RF 532 ($^{207}Pb/^{206}Pb$ = 1.33 ± 0.02 and $^{204}Pb/^{206}Pb$ = 0.0412 ± 0.002) to apply a lunar initial Pb correction to the $^{207}Pb/^{206}Pb$ values from the apatite U-Pb analyses. We find that our lunar initial Pb-corrected $^{207}Pb/^{206}Pb$ dates have a range of 3852 ± 41 to 3877 ± 45 Ma. It is impossible to say for sure what proportion of non-radiogenic Pb in a given analysis is lunar initial Pb *versus* terrestrial Pb, so if analyses with high $^{204}Pb/^{206}Pb$ (>0.001) are excluded, the weighted mean of the lunar initial corrected $^{207}Pb/^{206}Pb$ dates is 3862.2 ± 9.5 Ma (n = 11 out of 11 total analyses, MSWD = 0.23, p($\chi$2) = 0.99), in good agreement with the Pb-Pb isochron date from the crystalline clast.

## 4    Discussion

### 4.1    Grouping with the YAMM lunar meteorites

The YAMM meteorites, consisting of Y-793169, A-881757, MIL 05035, and MET 01210, are a group of lunar meteorites
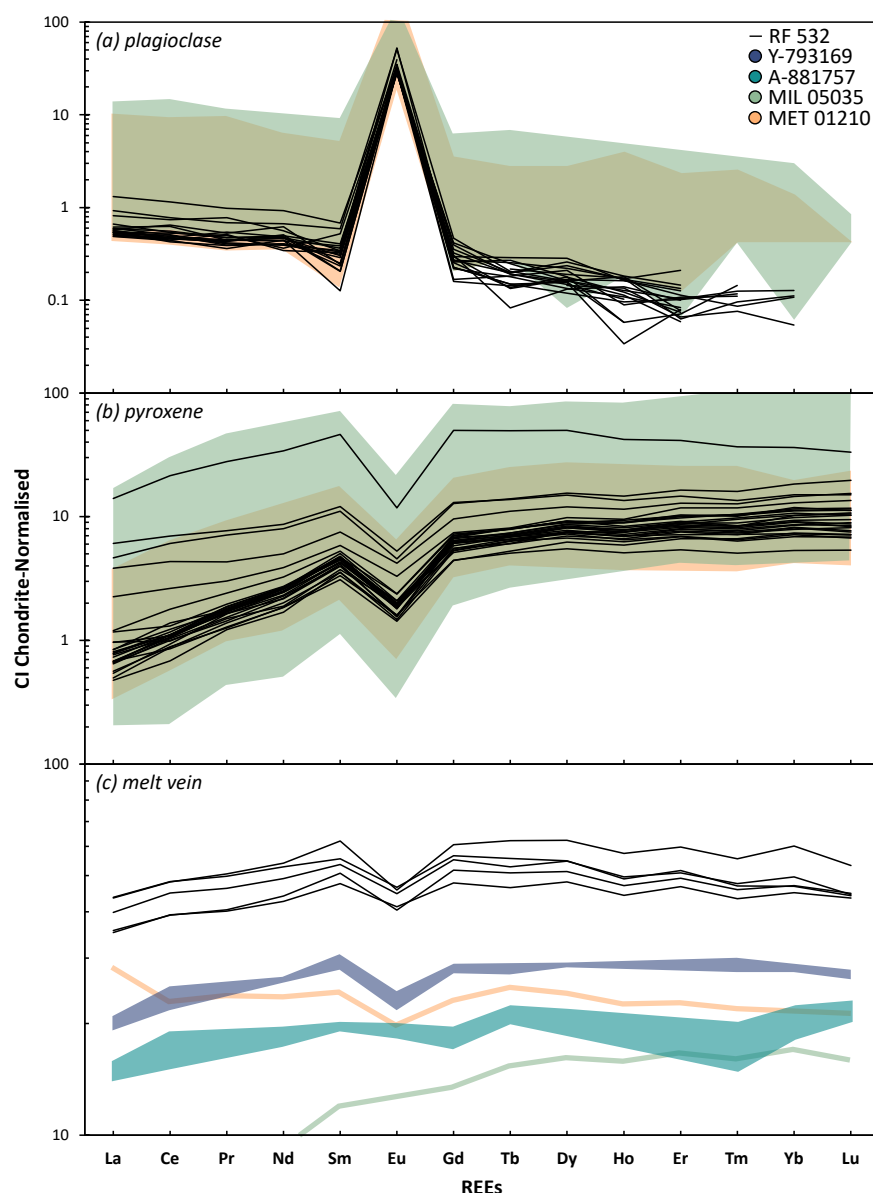
**Figure 6.** CI chondrite-normalised REE patterns for (a) plagioclase, (b) pyroxene, and (c) the melt vein in RF 532. In (c), the melt vein data for RF 532 is compared to bulk rock analyses of the YAMM meteorites. CI chondrite values are from Anders and Grevesse (1989), and literature data for the YAMM meteorites are from Jolliff et al. (1993); Koeberl et al. (1993); Korotev et al. (2003); Day et al. (2006a); Joy et al. (2008); Liu et al. (2009).

that are thought to be launch paired due to similarities in their petrology, mineralogy, geochemistry, and geochronology (Yanai, 1991; Yanai and Kojima, 1991; Jolliff et al., 1993; Koeberl et al., 1993; Takeda et al., 1993; Joy et al., 2008; Fernandes et al., 2009; Liu et al., 2009; Arai et al., 2010; Merle et al., 2024). With the discovery of RF 532 in 2018 (Gattacceca et al., 2022; and possible paired stone RF 535 in 2019; Gattacceca et al., 2025), it has been suggested that it is a new member of this group. As well, the recently recovered lunar gabbro NWA 16256 (Gattacceca et al., 2025) may be another member of the YAMM group, based on its mineralogical similarity with A-881757 and MIL 05035, but no detailed work on this sample has yet been published. It has also been proposed that Dominion Range (DOM) 18262 and paired stones are members of the YAMM group, with similarities to the MET 01210 regolith breccia, but again, no detailed work on this sample has yet been published.

Asuka 881757 is dominantly composed of large swaths of zoned and fractured pyroxene that surround and enclose solitary grains of maskelynitised plagioclase. Other phases include olivine, ilmenite, ulvöspinel, silica, and troilite, and olivine-pyroxene-silica symplectic intergrowths are common (Yanai, 1991; Yanai and Kojima, 1991; Jolliff et al., 1993; Koeberl et al., 1993). On average, plagioclase and pyroxene grains range in size from 1000–4000 µm (Yanai, 1991). Miller Range 05035 has a similar texture and mineralogy, and a slightly larger average grain size for plagioclase and pyroxene, with grains ranging from 2000–6000 µm (Joy et al., 2008). While Y-393169 and the MET 01210 basalt
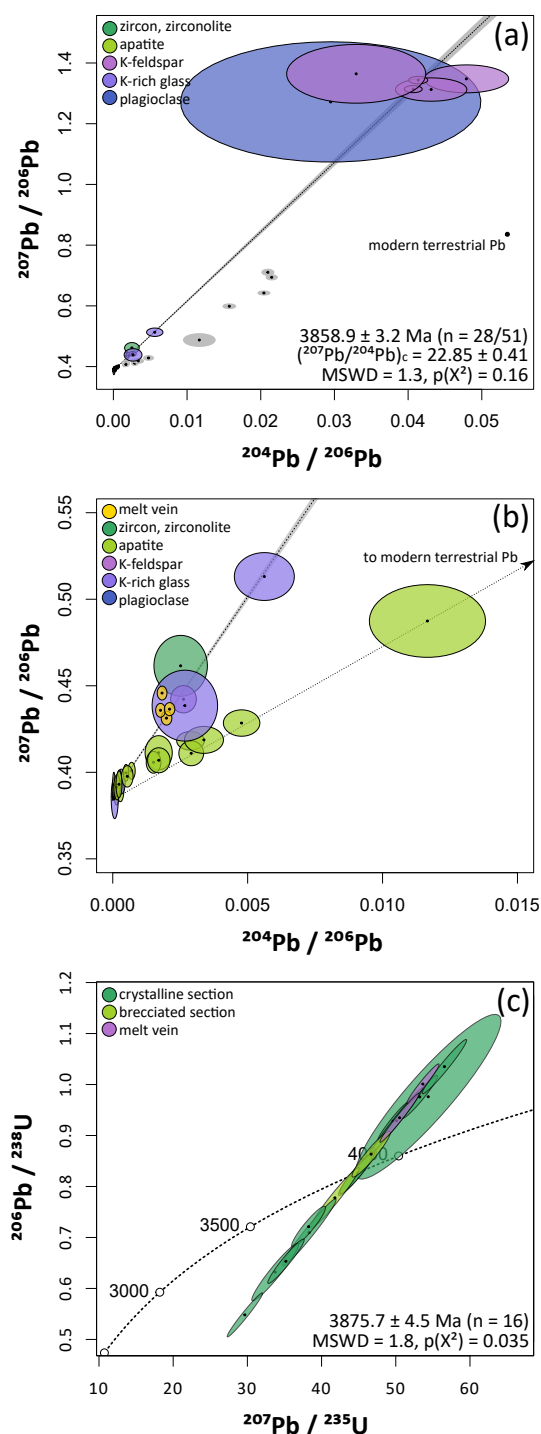
Figure 7. (a) $^{207}Pb/^{206}Pb$ vs. $^{204}Pb/^{206}Pb$ isochron for RF 532, with different mineral phases appearing as different colours. Grey data points that lie to the right of the isochron are analyses filtered out due to suspected terrestrial contamination, see the mixing relation with modern terrestrial Pb (Stacey and Kramers, 1975). (b) A zoomed in view of (a) with melt vein data and apatite data from our U-Pb session included as the data points veering towards modern terrestrial Pb. (c) $^{206}Pb/^{238}U$ vs. $^{207}Pb/^{235}U$ concordia plot for apatite grains in RF 532, with grains from different regions of the sample appearing in different colours.

clasts have a similar mineralogy, they have a smaller grain size, on the average of 1000–1500 µm (Takeda et al., 1993; Arai et al., 2010). Thus, RF 532, which contains coarse-grained plagioclase surrounded by zoned and fractured pyroxene, with an average grain size of 500 to >2500 µm (Figures 1, 2a,c), appears more similar to A-881757 and MIL 05035 than Y-793169 or the basalt clasts in MET 01210.

This is also reflected in the mineral chemistry of RF 532. Our analysis of RF 532 shows that it is a low-Ti gabbro (Figure 5), dominantly composed of anorthitic plagioclase (Figure 3) and augitic to pigeonitic pyroxene (Figure 4), much like the YAMM meteorites. Generally, our major and minor element mineral chemistry for RF 532 does not encompass as broad ranges as what has been recorded for the YAMM meteorites; however, this may be due to a more limited sampling of RF 532.

Chondrite-normalised REE patterns for plagioclase and pyroxene in RF 532 are more like those in MIL 05035 than in MET 01210. This is seen in Figure 6a-b, with analyses of plagioclase in RF 532 plotting closest to those derived for MIL 05035 and analyses of pyroxene plotting with higher REE abundances like some of those reported from MIL 05035 (Liu et al., 2009). REE patterns from the melt vein in RF 532 could, potentially, represent a pseudo bulk rock signature for the sample. They closely resemble bulk rock signatures derived for Y-793169 and A-881757, but with 2–3 × higher REE abundances (Figure 6).

A number of dates have been derived for the YAMM meteorites across multiple isotope systems (Table 1, Figure 8). Argon-argon dates range from 3763 ± 46 to 3910 ± 12 Ma (Misawa et al., 1993; Fernandes et al., 2009), Sm-Nd dates range from 3430 ± 190 to 3871 ± 57 Ma (Misawa et al., 1993; Torigoye-Kita et al., 1995; Thalmann et al., 1996), U-Pb dates range from 3810 ± 220 to 3940 ± 9 Ma (Misawa et al., 1993; Torigoye-Kita et al., 1995; Terada et al., 2007), Pb-Pb dates range from 3862.1 ± 4.5 to 3940 ± 28 Ma (Misawa et al., 1993; Torigoye-Kita et al., 1995; Terada et al., 2007; Zhang et al., 2010; Merle et al., 2024), and a Rb-Sr date is 3840 ± 32 Ma (Misawa et al., 1993).

Recently, Merle et al. (2024) applied the same in situ Pb isotope analysis protocol to A-881757 and MIL 05035. They obtained Pb-Pb isochron dates of 3864.8 ± 3.7 Ma for A-881757 and 3862.1 ± 4.5 Ma for MIL 05035, which are consistent within uncertainty with the Pb-Pb isochron date of 3858.9 ± 3.2 Ma we obtained for RF 532. Additionally, initial Pb compositions were calculated by Merle et al. (2024), which they then used to determine µ-values for the source of the original parent rock, where µ is the ratio $^{238}U/^{204}Pb$. Asuka 881757 had an initial $^{207}Pb/^{206}Pb$ of 1.317 ± 0.010, $^{204}Pb/^{206}Pb$ of 0.0403 ± 0.0015, and µ = 93 ± 9, while MIL 05035 had an initial $^{207}Pb/^{206}Pb$ of 1.211 ± 0.014, $^{204}Pb/^{206}Pb$ of 0.0354 ± 0.0025, and µ = 60 ± 54. Taking a single-stage model approach, we start from a Canyon Diablo Troilite (CDT) Pb isotope composition (Göpel et al., 1985) at the age of the Solar System, 4567 Ma (Connelly et al., 2012), and let it evolve until we reach the initial Pb composition of RF 532 ($^{207}Pb/^{206}Pb$ = 1.33 ± 0.02,

**Table 1.** A compilation of published ages (in Ma) for the YAMM meteorites. All uncertainties are quoted to 2σ. [a]This work, [b]Misawa et al. (1993), [c]Torigoye-Kita et al. (1995), [d]Thalmann et al. (1996), [e]Terada et al. (2007), [f]Fernandes et al. (2009), [g]Zhang et al. (2010), and [h]Merle et al. (2024).

| | RF 532 | Y-793169 | A-881757 | MIL 05035 | MET 01210 |
|---|---|---|---|---|---|
| U-Pb | | 3810 ± 220[c] | 3940 ± 9[b] | | 3899 ± 500[e] 3882 ± 130[e] |
| Pb-Pb | 3858.9 ± 3.2[a] | 3919 ± 94[c] | 3864.8 ± 3.7[h] 3940 ± 28[b] | 3862.1 ± 4.5[h] 3851 ± 8[g] | 3904 ± 85[e] |
| Ar-Ar | | 3811 ± 98[f] | 3763 ± 46[f] 3790 ± 16[b] | 3910 ± 12[f] | |
| Sm-Nd | | 3430 ± 190[c] | 3871 ± 57[b] | 3800 ± 50[d] | |
| Rb-Sr | | | 3840 ± 32[b] | | |

$^{204}Pb/^{206}Pb = 0.0412 \pm 0.002$) at its crystallisation age of 3858.9 ± 3.2 Ma. Following this logic, we find that RF 532 was derived from a source with a μ-value of 71 ± 6, which is much lower than what has been calculated for Apollo basalts (e.g., 360–390 for high-Ti basalts, 410–650 for low-Ti basalts; Snape et al., 2019). Following the multiple-stage Pb evolution approach of Merle et al. (2024) and Che et al. (2025), we calculate a μ-value of 81 ± 13. Our μ-value of ∼71–81 is similar to the value derived by Merle et al. (2024) for A-881757 and MIL 05035, thus, providing another degree of similarity to the YAMM meteorite group.

Therefore, based on remarkable similarities in petrology, mineralogy, major and trace element mineral chemistry, geochronology, and Pb isotope systematics, we suggest that RF 532 (and RF 535) is another member of the YAMM lunar meteorite group.

## 4.2 Geological history

### 4.2.1 Lava flow origins

The YAMM lunar meteorites are interpreted to have sampled a single basaltic lava flow and its overlying regolith (Joy et al., 2008; Arai et al., 2010). In a typical lava flow, cooling is slowest in the centre of the flow and faster nearer the surface. Thus, basalts generated in the centre of the flow will have a coarser texture than those generated at the margins. Asuka 881757 and MIL 05035, which have a slightly coarser grain size and less magnesian pyroxene cores than Y-793169 and the MET 01210 basalt clasts, likely originated from the central region of the lava flow, in the lower units described by Joy et al. (2008) and Arai et al. (2010). Meanwhile, Y-793169 and the MET 01210 basalt clasts, which have a slightly finer grain size and more magnesian pyroxene cores, likely originated near the surface of the lava flow (Joy et al., 2008; Arai et al., 2010). As identified by its petrology, mineralogy, and geochemistry, RF 532 is more similar to A-881757 and MIL 05035 than Y-793169 and MET 01210. Thus, the gabbroic component of RF 532 was likely generated nearer the centre of the lava flow, along with A-881757 and MIL 05035.

### 4.2.2 Post-crystallisation impact reprocessing

Following crystallisation, RF 532 was fractured *in situ*, as indicated by its monomict brecciated texture. Typically, in impact crater environments, monomict breccias occur in either the crater floor, crater fill, or the ejecta blanket (Stöffler et al., 1979, 2018). Melt pockets, melt veins, and vesicles like those seen in RF 532 (Figure 2e-h) can occur at shock pressures as low as ∼20 GPa, but are more common at higher shock pressures in basaltic samples (≥∼30 GPa; Stöffler et al., 2018). However, recent experimental studies on shock effects in terrestrial basalts suggest that the shock pressure required to form localised melt veins is lower than previously thought, on the order of ∼10–20 GPa for basaltic samples (e.g., eucrites; Ono et al., 2023). Maskelynite, a diaplectic glass, forms from plagioclase at shock pressures of ∼20–35 GPa depending on Ca concentration (Fritz et al., 2017; Stöffler et al., 2018). In RF 532, plagioclase has been *partly* maskelynitised, suggesting it only experienced the lower end of shock pressures, closer to ∼20 GPa. Overall, RF 532 likely only ever experienced shock pressures as high as ∼20–25 GPa.

In A-881757 and MIL 05035, plagioclase has been *fully* maskelynitised (Koeberl et al., 1993; Mikouchi, 1999; Joy et al., 2008; Arai et al., 2010), indicating these two samples have experienced higher shock pressures than RF 532. In Y-793169, plagioclase is either partly maskelynitised or recrystallised from diaplectic glass (Yanai, 1991; Takeda et al., 1993; Mikouchi, 1999), suggesting it may have experienced even higher shock pressures than A-881757 and MIL 05035. In the MET 01210 basalt clasts, plagioclase is chemically zoned and fractured but preserves a primary igneous texture (Arai et al., 2010); it may be similar to Y-793169 in that it has recrystallised from diaplectic glass and has experienced higher shock pressures. Microcrystals of coesite and stishovite are high pressure polymorphs of $SiO_2$ that have been found in A-881757, indicating it has experienced shock pressures from 8–30 GPa. However, the absence of seiferite means that pressures have not gone above 35 GPa (Ohtani et al., 2011). Additionally, Y-793169 and A-881757 are reported to have experienced diffusive loss of radiogenic $^4He$ and $^{40}Ar$ due to shock (Thalmann et al., 1996).

Uranium-lead dates obtained on apatite grains from both the melt vein and brecciated sections of RF 532 show negligible difference to those from the crystalline section, i.e., they are all within uncertainty (Figure 7b, Table S3.4 in Oliveira et al., 2025). This suggests that either the
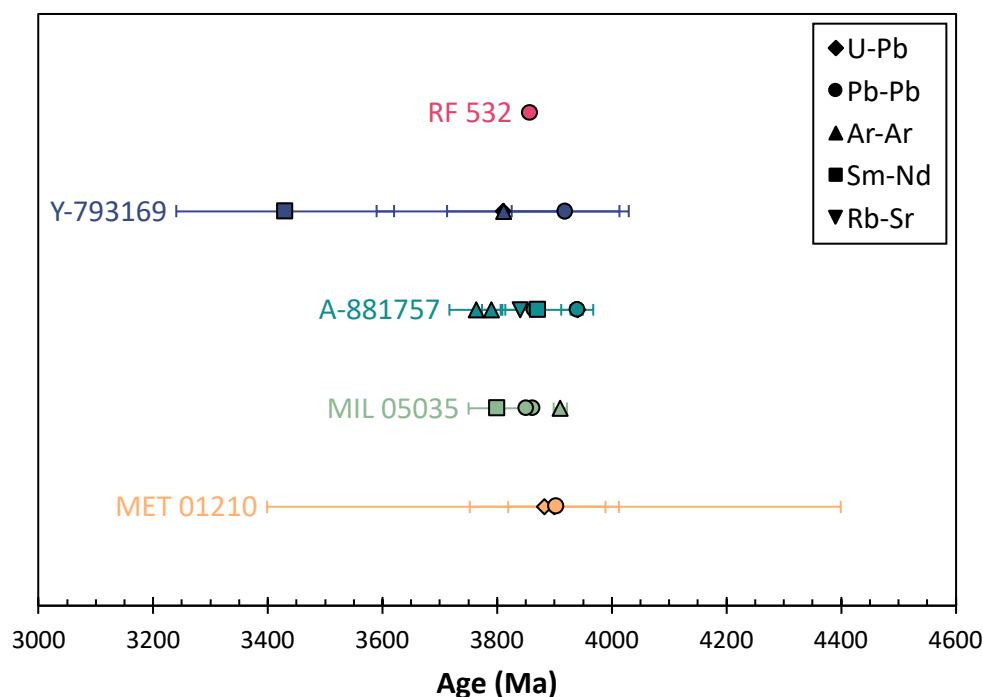
**Figure 8.** Summary of dates for RF 532 and the YAMM meteorites (see Table 1). Uncertainties are 2σ. Literature data for the YAMM meteorites are the same as those given in the Table 1 caption.

original igneous rock was impacted very soon after crystallisation, or that it did not experience shock pressures and temperatures high enough to disturb the U-Pb systematics in the apatite grains. In apatite, grains begin to show minor evidence of shock deformation at pressures of 15–20 GPa and significant evidence at pressures of 30–35 GPa (from Raman spectroscopy, cathodoluminescence imaging, and electron backscatter diffraction by Černok et al., 2019). Lead diffusion begins above closure temperatures of 375–600 °C and are dependent on grain size and duration of heating (Cochrane et al., 2014). For the apatite grains in RF 532, they were likely too large in size, not in a very hot ejecta blanket, and/or not in said ejecta blanket for a long enough duration to have experienced Pb diffusion via heating.

At some point following crystallisation, this lava flow was impacted during one or more events that disturbed some of its isotopic signatures. For example, Ar-Ar dates for the YAMM meteorites are slightly lower than those from other isotope systems (e.g., an Ar-Ar date of 3763 ± 46 Ma derived by Fernandes et al., 2009 *versus* a Pb-Pb date of 38648 ± 37 Ma derived by Merle et al., 2024), suggesting they may have been disturbed around 3763 Ma. This major isotopic resetting event could have generated some of the shock effects we see across the YAMM stones. Ramlat Fasad 532 may have been located on the Moon further from the impactor, resulting in its monomict brecciated texture, partly maskelynitised plagioclase, and melt pockets and veins. Asuka 881757 and MIL 05035 would have been closer to the impactor and, thus, experienced slightly higher shock pressures which preserved their igneous texture, but

fully maskelynitised the plagioclase grains. Yamato 793169 and the MET 01210 basalt clasts would have been sited closest to the surface of the lava flow and, thus, the impactor, experiencing the highest shock pressures that resulted in recrystallisation from diaplectic glass. Meteorite Hills 01210 was likely affected by multiple impactors, which took material from the upper portion of the lava flow and brought it to the surface, where it was mixed with more feldspathic material and consolidated into a regolith breccia (Joy et al., 2010).

### 4.2.3 Lunar ejection

Finally, the YAMM and RF 532 stones must have been launched off the Moon by a much younger impact event. Typically, lunar meteoroids have been ejected from small impact craters <1 km in diameter (Warren, 1994; Gladman et al., 1995, 1996; Basilevsky et al., 2010) at speeds of 2.38–3.40 km/s (Gladman et al., 1995, 1996). Cosmic ray exposure ages have not yet been established for RF 532, however, most lunar meteorite CRE ages indicate that their meteoroids were ejected off the Moon sometime in the past 100 ka, and all within the past 20 Ma (e.g., Lorenzetti et al., 2005; Basilevsky et al., 2010; Joy et al., 2023), which is also supported by modelling studies (Gladman et al., 1995, 1996). Cosmic ray exposure ages have been reported for the YAMM meteorites. Yamato 793169 was ejected from the Moon at 0.93 ± 0.20 Ma from a depth of ~500 g/cm$^2$ (Nishiizumi et al., 1992; Thalmann et al., 1996), which corresponds to a depth of ~1.5 m (using the bulk density calculated for MIL 05035; Kiefer et al., 2012). Similarly, A-881757 was ejected from the Moon at 0.83 ± 0.20 Ma from

a depth of $60 \text{ g/cm}^2$ or $\sim 0.2 \text{ m}$ (Nishiizumi et al., 1992; Thalmann et al., 1996), MIL 05035 at $0.75 \pm 0.14 \text{ Ma}$ from a depth of $>1000 \text{ g/cm}^2$ or $>3 \text{ m}$ (preliminary data from Nishiizumi and Caffee, 2013), and MET 01210 at $0.95 \pm 0.13 \text{ Ma}$ from a depth of $>1000 \text{ g/cm}^2$ or $>3 \text{ m}$ (preliminary data from Nishiizumi et al., 2006). These ejection ages are within uncertainty of each other (weighted average date of $0.86 \pm 0.20 \text{ Ma}$), suggesting that the YAMM stones (and presumably RF 532) were ejected in the same impact event at *ca.* 0.9 Ma (Figure 9). It is possible that RF 532 was ejected in a different impact event from the same or similar material, but until we derive CRE ages for it, we cannot be certain. For now, we assume that it was launched alongside the YAMM stones. The inferred depths for the YAMM stones are inconsistent with the proposed lava flow stratigraphy; prior to ejection off the Moon, impactors must have overturned some of the material, bringing parts of the lava flow to different depths over time where cosmogenic isotopes were generated.

Following their launch from the Moon, modelling indicates that lunar meteoroids typically spend <1 Ma in space before colliding with the Earth (if they will collide with the Earth, some lunar meteoroids will instead escape directly into heliocentric orbit where they will orbit the Sun; Gladman et al., 1995, 1996). This is supported by short transit times derived from CRE ages (Figure 9), however, these are often complex and can be difficult to interpret (Hidaka et al., 2017). Once on Earth, a lunar meteorite typically resides on the surface for <0.4 Ma before recovery (see discussion in Joy et al., 2023).

## 4.3 Transit to Earth

The YAMM meteorites originated from the same lava flow on the Moon. Thus, the grouping of RF 532 with the YAMM meteorites indicates that lunar material ejected from the same launch event can fall to Earth across multiple continents, which could have broader implications for the Moon-to-Earth meteorite delivery system. Other cross-continental lunar meteorite fall pairs/groups have been suggested before: for example, the 'YQEND' basaltic breccia meteorite group, consisting of Y-793274/981031, Queen Alexandra Range (QUE) 94281, Elephant Moraine (EET) 87521/96008, NWA 4884, NWA 7611, and Mount DeWitt (DEW) 12007 (Korotev and Zeigler, 2014; Joy et al., 2023). Another proposed cross-continental pair comprises the feldspathic MIL 090036 and NWA 7022 samples (Korotev and Irving, 2021). As well, there is the proposed 'NNL' basalt meteorite group, which consists of NWA 4734/10597, NWA 032/479, Northeast Africa (NEA) 003, and the LaPaz Icefield (LAP) basalts, LAP 02205/02224/02226/02436/03632/04841 (Zeigler et al., 2005; Korotev and Zeigler, 2014; Korotev and Irving, 2021; Joy et al., 2023). The LAP basalts constitute a fall group, however, if grouped with NWA 032/479, NWA 4734, and NEA 003, they would be denoted as a launch group due to the distance between their find locations (see Merle et al., 2020; Korotev and Irving, 2021). However, isotopic differences have been identified between some of the NNL stones, which suggests they may not sample the same lava flow (Elardo et al., 2014), but they may still sample material from the same source impact crater on the Moon.

For these groups of meteorites, some stones were recovered during systematic searching from icefields in Antarctica while others were sourced from meteorite dealers recovering material from Morrocco and other northwest African countries. Generally, lunar meteorites from north African countries have been obtained through indirect means and, thus, have poorly documented find circumstances and locations, rendering knowledge of their find site generally inaccurate and unreliable (Korotev and Irving, 2021). The advantage for RF 532 and the YAMM meteorites, then, is that all paired stones were recovered during systematic meteorite recovery programmes. Thus, all five stones have well documented circumstances and reported find locations, which include exact Earth coordinates.

Terrestrial residence ages have been determined for the YAMM stones: <0.05 Ma for Y-793169 and A-881757 (Nishiizumi et al., 1992), $0.07 \pm 0.06 \text{ Ma}$ for MIL 05035 (preliminary data from Nishiizumi and Caffee, 2013), and <0.02 Ma for MET 01210 (preliminary data from Nishiizumi et al., 2006). Similar ejection ages of *ca.* 0.8–0.9 Ma amongst the four YAMM stones support the suggestion that they were ejected from the Moon in the same launch event (Nishiizumi et al., 1992, 2006; Arai et al., 2010; Nishiizumi and Caffee, 2013), however, slight differences in terrestrial residence ages of *ca.* 0.02–0.07 Ma suggest that they may not have arrived on Earth in the same entry and fall event.

Typically, strewn fields (i.e., an area on Earth where stone(s) from a single meteor impact are dispersed, affected by parameters such as entry angle and velocity, trajectory, size and shape of the meteoroid, wind speed and direction, etc.; Svetsov, 1995; Collins et al., 2005) are only several to tens of kilometres in size and are rarely longer than 40 km (Li et al., 2022). The longest known meteorite strewn field is that of the Aletai iron meteorite, which has a length of $\sim 430 \text{ km}$, explained by a very shallow entry angle and 'skipping stone'-like trajectory of the arriving meteoroid (Li et al., 2022). The find locations between the Y-793169 and A-881757, and MIL 05035 and MET 01210 stones are $\sim 2500 \text{ km}$ and $\sim 2900 \text{ km}$ apart, respectively (Figure 10), which is far greater than that of the Aletai iron meteorites.

For Antarctic meteorites, there is another issue in the interpretation of their recovery coordinates in that ice sheets are not static. They constantly move, flowing outwards in all directions from the centre of the Antarctic Plateau, driven by their own weight and gravitational forces. This means that the geographical location where a meteorite is recovered in Antarctica is likely different to the location where it first fell. Indeed, meteorites that fell somewhere in the central polar plateau would likely be transported to 'blue ice areas' nearer the edges of the Antarctic continent (i.e., the meteorite transport conveyer belt model, Cassidy et al., 1992; Corti et al., 2003). These blue ice areas are atypical regions where meteorites have been exposed over time due to favourable ice flow and meteorological conditions. They are typically stagnant, meaning that meteorites may sit
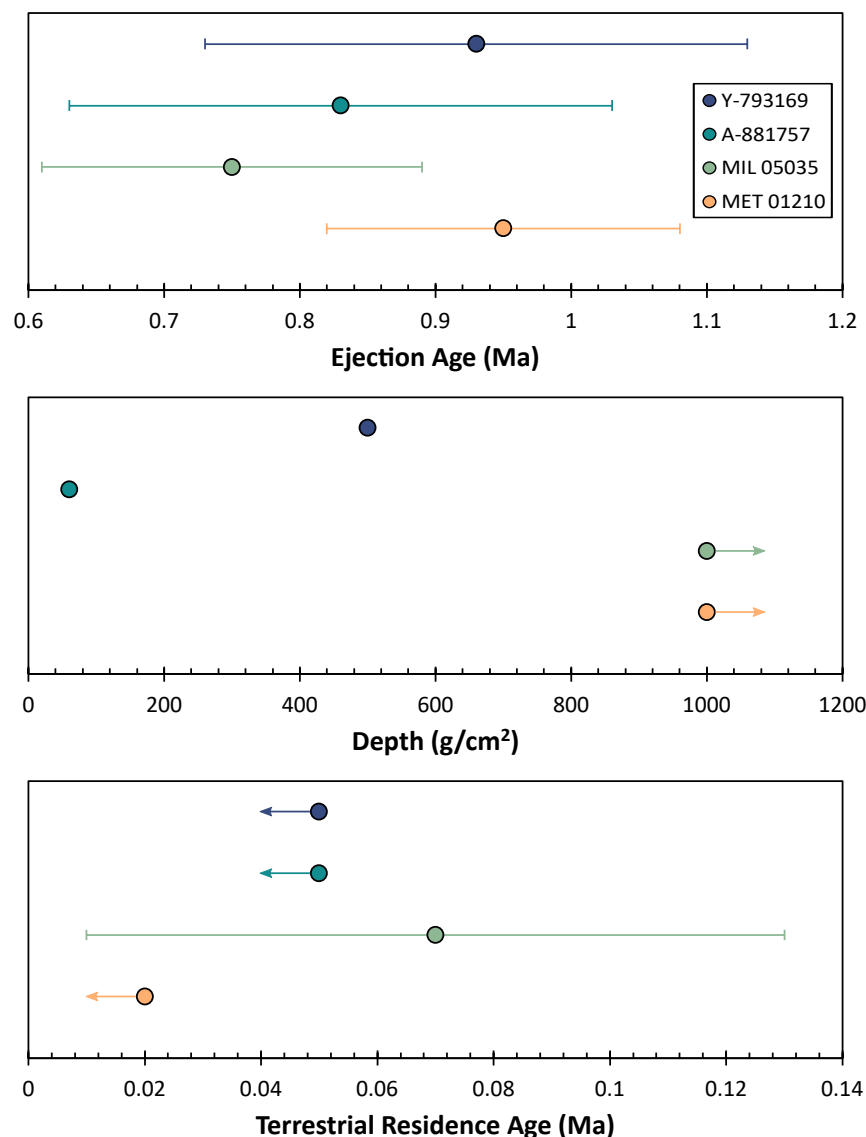
**Figure 9.** Summary of CRE ages, ejection depths, and terrestrial residence ages for the YAMM meteorites. Uncertainties are 2σ. Literature data are from Nishiizumi et al. (1992); Warren (1994); Thalmann et al. (1996); Nishiizumi et al. (2006); Nishiizumi and Caffee (2013).

exposed at the surface for thousands of years (Whillans and Cassidy, 1983; Tollenaar et al., 2024).

The Miller Range and Meteorite Hills blue ice areas are fed by the large Byrd Glacier and MacAyeal Ice Stream catchments, and the Yamato and Asuka blue ice areas are fed by the Princess Ragnhild coast glacier catchment (Figure 10a). These catchments are separated by ∼900 km and in-between there are two very large ice basins—the Recovery Icefield and the Lambert glacier, which feed ice elsewhere (i.e., towards the Weddell and Cooperation Seas). The sheer size of these two ice basins means that a single fall event for the YAMM stones in the central polar plateau is unlikely; to account for their find locations on opposite sides of the Antarctic continent, there must have been two (or more) fall events.

Additionally, age data for ice cores nearest the find locations for the YAMM stones indicates that there has been little movement since they fell. For example, an ice core from the South Yamato blue ice area (∼65 km from the recovery coordinates of Y-793169) has an age of ∼0.061 Ma at a depth of 100 m (Moore et al., 2006). The terrestrial residence age of <0.05 Ma for Y-793169 (Nishiizumi et al., 1992) is well within that of ∼0.061 Ma for the South Yamato blue ice area (Moore et al., 2006), suggesting that Y-793169 may not have been transported much since it fell. Samples of an ice core from the Taylor Glacier blue ice area (∼220 km from the recovery coordinates of MET 01210) have ages of ∼0.12 Ma at a 100 m depth (Buizert et al., 2014), in line with a terrestrial residence age of <0.02 Ma for MET 01210 (Nishiizumi et al., 2006), reinforcing this suggestion of ice stagnation.

By adding RF 532 to the YAMM meteorite group, with its find location over >10 000 km away in Oman (Figure 10b), we only reinforce the suggestion that they fell in multiple events over a period of tens of thousands of years (Nishiizumi et al., 1992, 2006; Nishiizumi and Caffee, 2013).
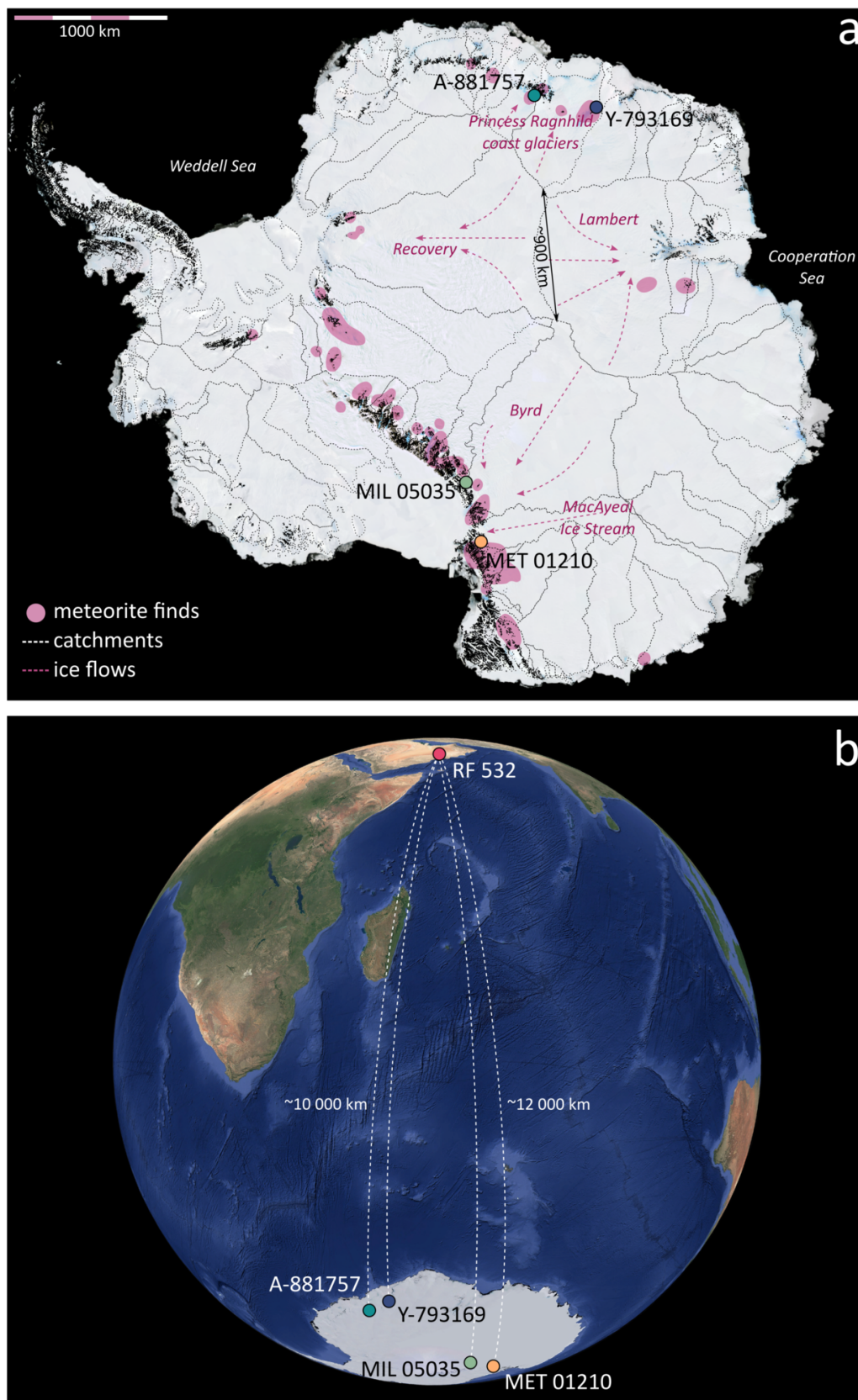
**Figure 10.** (a) Map of Antarctica showing the recovery locations for the YAMM stones (basemap from Bindschadler et al., 2008). Regions where meteorites have been found in Antarctica, ice catchments (Zwally et al., 2012; Willis et al., 2016), and relevant ice flow directions (Mouginot et al., 2019) are shown for reference. (b) Map showing the distances between the recovery locations of RF 532 in Oman and the YAMM meteorites in Antarctica (basemap from Google Earth, view from an altitude of ∼14 000 km).

## 5   Conclusion

Ramlat Fasad 532 is a lunar gabbroic monomict breccia, dominantly composed of anorthitic plagioclase and augitic to pigeonitic pyroxene. It has a monomict brecciated texture, where large crystalline clasts are set in a fragmented matrix of the same mineralogical composition, with melt pockets and veins as common constituents.

Our detailed characterisation of RF 532 shows that it is grouped with the YAMM lunar meteorite group, and, together, they sample a low-Ti basaltic lava flow and its overlying regolith. Ramlat Fasad 532 crystallised in the lower, more central region of the lava flow at 3858.9 ± 3.2 Ma, along with A-881757 and MIL 05035, while Y-793169 and the MET 01210 basalt components crystallised closer to the surface. Following crystallisation, the lava flow was struck by one or more impactor(s) (evidenced by younger Ar-Ar ages for the YAMM stones), with RF 532 being more distal from the impactor than the other YAMM stones, resulting in less severe shock effects (e.g., monomict brecciation, partial maskelynitisation).

Ramlat Fasad 532 and the YAMM group become the first cross-continental lunar meteorite group where *all* the individual stones were recovered during systematic scientific expedition searching and, thus, have precise Earth recovery coordinates for *all* stones. The individual stones did not likely fall to Earth at the same time and instead fell over a period of tens of thousands of years. Deriving CRE and terrestrial residence ages for RF 532 would be useful to fully investigate the launch and transit history of this grouping, allowing us to explore whether they align with the rest of the YAMM stones. Even then, some exposure ages have significant uncertainties (e.g., terrestrial residence ages), and until they can be determined to a higher degree of accuracy, it is difficult to decisively determine how lunar meteorites travel from the Moon to Earth. Models have been made to explore typical pathways (e.g., Gladman et al., 1995, 1996), with most lunar ejecta escaping the Moon at speeds of ~2.38–3.40 km/s (Gladman et al., 1995, 1996) from relatively small craters <1 km in diameter (Basilevsky et al., 2010) and arriving on Earth within 10–20 Ma (Joy et al., 2023). Still, being the first cross-continental pair with precise recovery coordinates, RF 532 and the YAMM group could be useful in future studies on the dynamics of the Moon-to-Earth lunar meteorite delivery system.

## Acknowledgements

## Data, code, and outputs availability

Analytical data are published in Oliveira et al. (2025, https://doi.org/10.48420/28902935.v1). Main text figures and table are available for download in the online version of this article.

## Licence agreement

## References

Anders E, Grevesse N (1989). Abundances of the elements: Meteoritic and solar. *Geochimica et Cosmochimica Acta* 53(1): 197–214. doi:10.1016/0016-7037(89)90286-x.

Arai T, Ray Hawke B, Giguere TA, Misawa K, Miyamoto M, Kojima H (2010). Antarctic lunar meteorites Yamato-793169, Asuka-881757, MIL 05035, and MET 01210 (YAMM): Launch pairing and possible cryptomare origin. *Geochimica et Cosmochimica Acta* 74(7): 2231–2248. doi:10.1016/j.gca.2009.11.019.

Arai T, Warren PH, Takeda H (1996). Four lunar mare meteorites: Crystallization trends of pyroxenes and spinels. *Meteoritics & Planetary Science* 31(6): 877–892. doi:10.1111/j.1945-5100.1996.tb02121.x.

Basilevsky A, Neukum G, Nyquist L (2010). The spatial and temporal distribution of lunar mare basalts as deduced from analysis of data for lunar meteorites. *Planetary and Space Science* 58(14–15): 1900–1905. doi:10.1016/j.pss.2010.08.020.

Bence AE, Papike JJ (1972). Pyroxenes as recorders of lunar basalt petrogenesis: Chemical trends due to crystal-liquid interaction. In *Proceedings of the 3rd Lunar Science Conference*, vol. 1, pp. 431–469. The M.I.T. Press. bibcode:1972LPSC....3..431B.

Bindschadler R, Vornberger P, Fleming A, Fox A, Mullins J, Binnie D, Paulsen S, Granneman B, Gorodetzky D (2008). The Landsat Image Mosaic of Antarctica. *Remote Sensing of Environment* 112(12): 4214–4226. doi:10.1016/j.rse.2008.07.006.

Buizert C, Baggenstos D, Jiang W, Purtschert R, Petrenko VV, Lu ZT, Müller P, Kuhl T, Lee J, Severinghaus JP, Brook EJ (2014). Radiometric [81]Kr dating identifies 120,000-year-old ice at Taylor Glacier, Antarctica. *Proceedings of the National Academy of Sciences* 111(19): 6876–6881. doi:10.1073/pnas.1320329111.

Cassidy W, Harvey R, Schutt J, Delisle G, Yanai K (1992). The meteorite collection sites of Antarctica. *Meteoritics* 27(5): 490–525. doi:10.1111/j.1945-5100.1992.tb01073.x.

Černok A, White LF, Darling J, Dunlop J, Anand M (2019). Shock-induced microtextures in lunar apatite and merrillite. *Meteoritics & Planetary Science* 54(6): 1262–1282. doi:10.1111/maps.13278.

Che X, Long T, Nemchin A, Xie S, Qiao L, Li Z, Ban Y, Fan R, Yang C, Liu D (2025). Isotopic and compositional constraints on the source of basalt collected from the lunar farside. *Science* 387(6740): 1306–1310. doi:10.1126/science.adt3332.

Cochrane R, Spikings RA, Chew D, Wotzlaw JF, Chiaradia M, Tyrrell S, Schaltegger U, Van der Lelij R (2014). High temperature (>350°C) thermochronology and mechanisms of Pb loss in apatite. *Geochimica et Cosmochimica Acta* 127: 39–56. doi:10.1016/j.gca.2013.11.028.

Collins GS, Melosh HJ, Marcus RA (2005). Earth Impact Effects Program: A Web-based computer program for calculating the regional environmental consequences of a meteoroid impact on Earth. *Meteoritics & Planetary Science* 40(6): 817–840. doi:10.1111/j.1945-5100.2005.tb00157.x.

Connelly JN, Bizzarro M, Krot AN, Nordlund Å, Wielandt D, Ivanova MA (2012). The Absolute Chronology and Thermal Processing of Solids in the Solar Protoplanetary Disk. *Science* 338(6107): 651–655. doi:10.1126/science.1226919.

Connolly HC, Smith C, Benedix G, Folco L, Righter K, Zipfel J, Yamaguchi A, Aoudjehane HC (2007). The Meteoritical Bulletin, No. 92, 2007 September. *Meteoritics & Planetary Science* 42(9): 1647–1694. doi:10.1111/j.1945-5100.2007.tb00596.x.

Corti G, Zeoli A, Bonini M (2003). Ice-flow dynamics and meteorite collection in Antarctica. *Earth and Planetary Science Letters* 215(3–4): 371–378. doi:10.1016/s0012-821x(03)00440-0.

Day JM, Floss C, Taylor LA, Anand M, Patchen AD (2006a). Evolved mare basalt magmatism, high Mg/Fe feldspathic crust, chondritic impactors, and the petrogenesis of Antarctic lunar breccia meteorite Meteorite Hills 01210 and Pecora Escarpment 02007. *Geochimica et Cosmochimica Acta* 70(24): 5957–5989. doi:10.1016/j.gca.2006.05.001.

Day JM, Taylor LA, Floss C, Patchen AD, Schnare DW, Pearson DG (2006b). Comparative petrology, geochemistry, and petrogenesis of evolved, low-Ti lunar mare basalt meteorites from the LaPaz Icefield, Antarctica. *Geochimica et Cosmochimica Acta* 70(6): 1581–1600. doi:10.1016/j.gca.2005.11.015.

Dymek RF, Albee AL, Chodos AA (1975). Comparative mineralogy and petrology of Apollo 17 mare basalts: samples 70215, 71055, 74255, and 75055. In *Proceedings of the 6th Lunar Science Conference*, pp. 49–77. New York, Pergamon Press, Inc., Houston, Texas, U.S.A. bibcode:1975LPSC....6...49D.

Elardo SM, Shearer CK, Fagan AL, Borg LE, Gaffney AM, Burger PV, Neal CR, Fernandes VA, McCubbin FM (2014). The origin of young mare basalts inferred from lunar meteorites Northwest Africa 4734, 032, and LaPaz Icefield 02205. *Meteoritics & Planetary Science* 49(2): 261–291. doi:10.1111/maps.12239.

Fernandes VA, Burgess R, Morris A (2009). $^{40}$Ar-$^{39}$Ar age determinations of lunar basalt meteorites Asuka 881757, Yamato 793169, Miller Range 05035, La Paz Icefield 02205, Northwest Africa 479, and basaltic breccia Elephant Moraine 96008. *Meteoritics & Planetary Science* 44(6): 805–821. doi:10.1111/j.1945-5100.2009.tb00770.x.

Fritz J (2012). Impact ejection of lunar meteorites and the age of Giordano Bruno. *Icarus* 221(2): 1183–1186. doi:10.1016/j.icarus.2012.08.019.

Fritz J, Greshake A, Fernandes VA (2017). Revising the shock classification of meteorites. *Meteoritics & Planetary Science* 52(6): 1216–1232. doi:10.1111/maps.12845.

Gattacceca J, McCubbin FM, Grossman J, Bouvier A, Chabot NL, D'Orazio M, Goodrich C, Greshake A, Gross J, Komatsu M, Miao B, Schrader D (2022). The Meteoritical Bulletin, No. 110. *Meteoritics & Planetary Science* 57(11): 2102–2105. doi:10.1111/maps.13918.

Gattacceca J, McCubbin FM, Grossman JN, Schrader DL, Cartier C, Consolmagno G, Goodrich C, Greshake A, Gross J, Joy KH, Miao B, Zhang B (2025). The Meteoritical Bulletin, No. 113. *Meteoritics & Planetary Science* 60(7): 1587–1591. doi:10.1111/maps.14374.

Gladman BJ, Burns JA, Duncan M, Lee P, Levison HF (1996). The Exchange of Impact Ejecta Between Terrestrial Planets. *Science* 271(5254): 1387–1392. doi:10.1126/science.271.5254.1387.

Gladman BJ, Burns JA, Duncan MJ, Levison HF (1995). The Dynamical Evolution of Lunar Impact Ejecta. *Icarus* 118(2): 302–321. doi:10.1006/icar.1995.1193.

Göpel C, Manhès G, Allègre C (1985). U-Pb systematics in iron meteorites: Uniformity of primordial lead. *Geochimica et Cosmochimica Acta* 49(8): 1681–1695. doi:10.1016/0016-7037(85)90139-5.

Hidaka H, Sakuma K, Nishiizumi K, Yoneda S (2017). Isotopic Evidence for Multi-stage Cosmic-ray Exposure Histories of Lunar Meteorites: Long Residence on the Moon and Short Transition to the Earth. *The Astronomical Journal* 153(6): 274. doi:10.3847/1538-3881/aa7139.

Hiess J, Condon DJ, McLean N, Noble SR (2012). 238U/235U Systematics in Terrestrial Uranium-Bearing Minerals. *Science* 335(6076): 1610–1614. doi:10.1126/science.1215507.

Hill E, Taylor LA, Floss C, Liu Y (2009). Lunar meteorite LaPaz Icefield 04841: Petrology, texture, and impact-shock effects of a low-Ti mare basalt. *Meteoritics & Planetary Science* 44(1): 87–94. doi:10.1111/j.1945-5100.2009.tb00719.x.

Jaffey AH, Flynn KF, Glendenin LE, Bentley WC, Essling AM (1971). Precision Measurement of Half-Lives and Specific Activities of U 235 and U 238. *Physical Review C* 4(5): 1889–1906. doi:10.1103/physrevc.4.1889.

Jarosewich E, Nelen JA, Norberg JA (1980a). Corrections. *Geostandards Newsletter* 4(2): 257–258. doi:10.1111/j.1751-908X.1980.tb00296.x.

Jarosewich E, Nelen JA, Norberg JA (1980b). Reference Samples for Electron Microprobe Analysis. *Geostandards Newsletter* 4(1): 43–47. doi:10.1111/j.1751-908x.1980.tb00273.x.

Jochum KP, Wilson SA, Abouchami W, Amini M, Chmeleff J, Eisenhauer A, Hegner E, Iaccheri LM, Kieffer B, Krause J, McDonough WF, Mertz-Kraus R, Raczek I, Rudnick RL, Scholz D, Steinhoefel G, Stoll B, Stracke A, Tonarini S, Weis D, Weis U, Woodhead JD (2011). GSD-1G and MPI-DING Reference Glasses for In Situ and Bulk Isotopic Determination. *Geostandards and Geoanalytical Research* 35(2): 193–226. doi:10.1111/j.1751-908x.2010.00114.x.

Jolliff BL, Korotev RL, Haskin LA (1993). Lunar basaltic meteorites Yamato-793169 and Asuka-881757: Samples of the same low-Ti mare-lava? *18th Symposium on Antarctic Meteorites* pp. 214–217.

Joy K, Crawford I, Anand M, Greenwood R, Franchi I, Russell S (2008). The petrology and geochemistry of Miller Range 05035: A new lunar gabbroic meteorite. *Geochimica et Cosmochimica Acta* 72(15): 3822–3844. doi:10.1016/j.gca.2008.04.032.

Joy KH, Crawford IA, Downes H, Russell SS, Kearsley AT (2006). A petrological, mineralogical, and chemical analysis of the lunar mare basalt meteorite LaPaz Icefield 02205, 02224, and 02226. *Meteoritics & Planetary Science* 41(7): 1003–1025. doi:10.1111/j.1945-5100.2006.tb00500.x.

Joy KH, Crawford IA, Russell SS, Kearsley AT (2010). Lunar meteorite regolith breccias: An in situ study of impact melt composition using LA-ICP-MS with implications for the composition of the lunar crust: Lunar meteorite regolith breccias. *Meteoritics & Planetary Science* 45(6): 917–946. doi:10.1111/j.1945-5100.2010.01067.x.

Joy KH, Gross J, Korotev RL, Zeigler RA, McCubbin FM, Snape JF, Curran NM, Pernet-Fisher JF, Arai T (2023). Lunar Meteorites. *Reviews in Mineralogy and Geochemistry* 89(1): 509–562. doi:10.2138/rmg.2023.89.12.

Kennedy AK, Wotzlaw J, Crowley JL, Schmitz M, Schaltegger U, Wade B, Martin L, Talavera C, Ware B, Bui TH (2023). Apatite Reference Materials for SIMS Microanalysis of Isotopes and Trace Elements. *Geostandards and Geoanalytical Research* 47(2): 373–402. doi:10.1111/ggr.12477.

Kiefer WS, Macke RJ, Britt DT, Irving AJ, Consolmagno GJ (2012). The density and porosity of lunar rocks. *Geophysical Research Letters* 39(7). doi:10.1029/2012gl051319.

Koeberl C, Kurat G, Brandstätter F (1993). Gabbroic lunar mare meteorites Asuka-881757 (Asuka-31) and Yamato-793169: Geochemical and mineralogical study. *Antarctic Meteorite Research* 6: 14–34. bibcode:1993AMR.....6...14K.

Korotev RL, Irving AJ (2021). Lunar meteorites from northern Africa. *Meteoritics & Planetary Science* 56(2): 206–240. doi:10.1111/maps.13617.

Korotev RL, Jolliff BL, Zeigler RA, Haskin LA (2003). Compositional constraints on the launch pairing of the three brecciated lunar meteorites of basaltic composition. *Antarctic Meteorite Research* 16: 152–175. bibcode:2003AMR....16..152K.

Korotev RL, Zeigler RA (2014). ANSMET Meteorites from the Moon. doi:10.1002/9781118798478.ch6.

Li Y, Li B, Hsu W, Jull AJT, Liao S, Zhao Y, Zhao H, Wu Y, Li S, Tang C (2022). A unique stone skipping–like trajectory of asteroid Aletai. *Science Advances* 8(25). doi:10.1126/sciadv.abm8890.

Liu Y, Floss C, Day JMD, Hill E, Taylor LA (2009). Petrogenesis of lunar mare basalt meteorite Miller Range 05035. *Meteoritics & Planetary Science* 44(2): 261–284. doi:10.1111/j.1945-5100.2009.tb00733.x.

Lorenzetti S, Busemann H, Eugster O (2005). Regolith history of lunar meteorites. *Meteoritics & Planetary Science* 40(2): 315–327. doi:10.1111/j.1945-5100.2005.tb00383.x.

Merle RE, Nemchin AA, Whitehouse MJ, Kenny GG, Snape JF (2024). Pb Isotope Signature of a Low-μ (238U/204Pb) Lunar Mantle Component. *Journal of Petrology* 65(6). doi:10.1093/petrology/egae062.

Merle RE, Nemchin AA, Whitehouse MJ, Snape JF, Kenny GG, Bellucci JJ, Connelly JN, Bizzarro M (2020). Pb-Pb ages and initial Pb isotopic composition of lunar meteorites: NWA 773 clan, NWA 4734, and Dhofar 287. *Meteoritics & Planetary Science* 55(8). doi:10.1111/maps.13547.

Mikouchi T (1999). Shocked plagioclase in the lunar meteorites Yamato-793169 and Asuka-881757: Implications for their shock and thermal histories. *Antarctic Meteorite Research* 12: 151–167. bibcode:1999AMR....12..151M.

Misawa K, Tatsumoto M, Dalrymple G, Yanai K (1993). An extremely low U/Pb source in the Moon: U-Th-Pb, Sm-Nd, Rb-Sr, and 40Ar/39Ar isotopic systematics and age of lunar meteorite Asuka 881757. *Geochimica et Cosmochimica Acta* 57(19): 4687–4702. doi:10.1016/0016-7037(93)90193-z.

Moore JC, Nishio F, Fujita S, Narita H, Pasteur E, Grinsted A, Sinisalo A, Maeno N (2006). Interpreting ancient ice in a shallow ice core from the South Yamato (Antarctica) blue ice area using flow modeling and compositional matching to deep ice cores. *Journal of Geophysical Research: Atmospheres* 111(D16). doi:10.1029/2005jd006343.

Mouginot J, Rignot E, Scheuchl B (2019). Continent-Wide, Interferometric SAR Phase, Mapping of Antarctic Ice Velocity. *Geophysical Research Letters* 46(16): 9710–9718. doi:10.1029/2019gl083826.

Mészáros M, Leya I, Hofmann BA (2017). Cosmic-ray exposure histories of the lunar meteorites AaU 012 and Shişr 166. *Meteoritics & Planetary Science* 52(9): 2040–2050. doi:10.1111/maps.12904.

Nemchin AA, Long T, Jolliff BL, Wan Y, Snape JF, Zeigler R, Grange ML, Liu D, Whitehouse MJ, Timms NE, Jourdan F (2021). Ages of lunar impact breccias: Limits for timing of the Imbrium impact. *Geochemistry* 81(1): 125683. doi:10.1016/j.chemer.2020.125683.

Nishiizumi K, Arnold JR, Caffee MW, Finkel CR, Reedy CR (1992). Cosmic ray exposure histories of lunar meteorites Asuka-881757, Yamato-793169, and Calcalong Creek. *17th symposium on Antarctic Meteorites* pp. 129–132. bibcode:1992anme...17..129N.

Nishiizumi K, Caffee MW (2013). Relationships among six lunar meteorites from Miller Range, Antarctica based on cosmogenic radionuclides (Abstract #2715). *Lunar and Planetary Science Conference* 44th.

Nishiizumi K, Hillegonds DJ, Welten KC (2006). Exposure and terrestrial histories of lunar meteorites LAP 02205/02224/02226/02436, MET 01210, and PCA 02007 (Abstract #2369). *Lunar and Planetary Science* 37th.

Ohtani E, Ozawa S, Miyahara M, Ito Y, Mikouchi T, Kimura M, Arai T, Sato K, Hiraga K (2011). Coesite and stishovite in a shocked lunar meteorite, Asuka-881757, and impact events in lunar surface. *Proceedings of the National Academy of Sciences* 108(2): 463–466. doi:10.1073/pnas.1009338108.

Oliveira B, Snape J, Tartese R, Joy K (2025). Mineral geochemistry and U-Th-Pb isotope systematics of the Ramlat Fasad 532 gabbroic lunar meteorite. University of Manchester. doi:10.48420/28902935.v1.

Ono H, Kurosawa K, Niihara T, Mikouchi T, Tomioka N, Isa J, Kagi H, Matsuzaki T, Sakuma H, Genda H, Sakaiya T, Kondo T, Kayama M, Koike M, Sano Y, Murayama M, Satake W, Matsui T (2023). Experimentally Shock-Induced Melt Veins in Basalt: Improving the Shock Classification of Eucrites. *Geophysical Research Letters* 50(1). doi:10.1029/2022gl101009.

Paquet M, Moynier F, Sossi PA, Dai W, Day JM (2025). Volatile loss history of the Moon from the copper isotopic compositions of mare basalts. *Earth and Planetary Science Letters* 656: 119250. doi:10.1016/j.epsl.2025.119250.

Paton C, Hellstrom J, Paul B, Woodhead J, Hergt J (2011). Iolite: Freeware for the visualisation and processing of mass spectrometric data. *Journal of Analytical Atomic Spectrometry* 26(12): 2508. doi:10.1039/c1ja10172b.

Righter K, Collins SJ, Brandon AD (2005). Mineralogy and petrology of the LaPaz Icefield lunar mare basaltic meteorites. *Meteoritics & Planetary Science* 40(11): 1703–1722. doi:10.1111/j.1945-5100.2005.tb00139.x.

Russell SS, Folco L, Grady MM, Zolensky ME, Jones R, Righter K, Zipfel J, Grossman JN (2004). The Meteoritical Bulletin, No. 88, 2004 July. *Meteoritics & Planetary Science* 39(S8). doi:10.1111/j.1945-5100.2004.tb00357.x.

Snape JF, Nemchin AA, Bellucci JJ, Whitehouse MJ, Tartèse R, Barnes JJ, Anand M, Crawford IA, Joy KH (2016). Lunar basalt chronology, mantle differentiation and implications for determining the age of the Moon. *Earth and Planetary Science Letters* 451: 149–158. doi:10.1016/j.epsl.2016.07.026.

Snape JF, Nemchin AA, Whitehouse MJ, Merle RE, Hopkinson T, Anand M (2019). The timing of basaltic volcanism at the Apollo landing sites. *Geochimica et Cosmochimica Acta* 266: 29–53. doi:10.1016/j.gca.2019.07.042.

Stacey J, Kramers J (1975). Approximation of terrestrial lead isotope evolution by a two-stage model. *Earth and Planetary Science Letters* 26(2): 207–221. doi:10.1016/0012-821x(75)90088-6.

Steiger R, Jäger E (1977). Subcommission on geochronology: Convention on the use of decay constants in geo- and cosmochronology. *Earth and Planetary Science Letters* 36(3): 359–362. doi:10.1016/0012-821x(77)90060-7.

Stöffler D, Hamann C, Metzler K (2018). Shock metamorphism of planetary silicate rocks and sediments: Proposal for an updated classification system. *Meteoritics & Planetary Science* 53(1): 5–49. doi:10.1111/maps.12912.

Stöffler D, Knöll HD, Maerz U (1979). Terrestrial and lunar impact breccias and the classification of lunar highland rocks. *Lunar and Planetary Science Conference Proceedings* 1: 639–675. bibcode:1979LPSC...10..639S.

Svetsov V (1995). Disintegration of Large Meteoroids in Earth's Atmosphere: Theoretical Models. *Icarus* 116(1): 131–153. doi:10.1006/icar.1995.1116.

Takeda H, Arai T, Saiki K (1993). Mineralogical studies of lunar meteorite Yamato-793169, a mare basalt. *Antarctic Meteorite Research* 6: 3–13. bibcode:1993AMR.....6....3T.

Terada K, Sasaki Y, Anand M, Joy KH, Sano Y (2007). Uranium–lead systematics of phosphates in lunar basaltic regolith breccia, Meteorite Hills 01210. *Earth and Planetary Science Letters* 259(1–2): 77–84. doi:10.1016/j.epsl.2007.04.029.

Thalmann C, Eugster O, Herzog GF, Xue S, Klein J, Krähenbühl U, Vogt S (1996). History of lunar meteorites Queen Alexandra Range 93069, Asuka 881757, and Yamato 793169 based on noble gas isotopic abundances, radionuclide concentrations, and chemical composition. *Meteoritics & Planetary Science* 31(6): 857–868. doi:10.1111/j.1945-5100.1996.tb02119.x.

Thiessen F, Nemchin A, Snape J, Bellucci J, Whitehouse M (2018). Apollo 12 breccia 12013: Impact-induced partial Pb loss in zircon and its implications for lunar geochronology. *Geochimica et Cosmochimica Acta* 230: 94–111. doi:10.1016/j.gca.2018.03.023.

Thiessen F, Nemchin AA, Snape JF, Whitehouse MJ, Bellucci JJ (2017). Impact history of the Apollo 17 landing site revealed by U-Pb SIMS ages. *Meteoritics & Planetary Science* 52(4): 584–611. doi:10.1111/maps.12814.

Tollenaar V, Zekollari H, Kittel C, Farinotti D, Lhermitte S, Debaille V, Goderis S, Claeys P, Joy KH, Pattyn F (2024). Antarctic meteorites threatened by climate warming. *Nature Climate Change* 14(4): 340–343. doi:10.1038/s41558-024-01954-y.

Torigoye-Kita N, Misawa K, Dalrymple G, Tatsumoto M (1995). Further evidence for a low U/Pb source in the moon: U-Th-Pb, Sm-Nd, and Ar-Ar isotopic systematics of lunar meteorite Yamato-793169. *Geochimica et Cosmochimica Acta* 59(12): 2621–2632. doi:10.1016/0016-7037(95)00154-9.

Vaniman DT, Papike JJ (1977). Very low Ti (VLT) basalts: A new mare rock type from the Apollo 17 drill core. In *Proceedings of the 8th Lunar Science Conference*, pp. 1443–1471. New York, Pergamon Press, Inc., Houston, Texas, U.S.A. bibcode:1977LPSC....8.1443V.

Vermeesch P (2018). IsoplotR: A free and open toolbox for geochronology. *Geoscience Frontiers* 9(5): 1479–1493. doi:10.1016/j.gsf.2018.04.001.

Wang Y, Hsu W, Guan Y, Li X, Li Q, Liu Y, Tang G (2012). Petrogenesis of the Northwest Africa 4734 basaltic lunar meteorite. *Geochimica et Cosmochimica Acta* 92: 329–344. doi:10.1016/j.gca.2012.06.024.

Warren PH (1994). Lunar and Martian Meteorite Delivery Services. *Icarus* 111(2): 338–363. doi:10.1006/icar.1994.1149.

Welten KC, Nishiizumi K, Caffee MW, Hillegonds DJ, Johnson JA, Jull AJT, Wieler R, Folco L (2006). Terrestrial ages, pairing, and concentration mechanism of Antarctic chondrites from Frontier Mountain, Northern Victoria Land. *Meteoritics & Planetary Science* 41(7): 1081–1094. doi:10.1111/j.1945-5100.2006.tb00506.x.

Whillans IM, Cassidy WA (1983). Catch a Falling Star: Meteorites and Old Ice. *Science* 222(4619): 55–57. doi:10.1126/science.222.4619.55.

Willis IC, Pope EL, Leysinger Vieli GJM, Arnold NS, Long S (2016). Drainage networks, lakes and water fluxes beneath the Antarctic ice sheet. *Annals of Glaciology* 57(72): 96–108. doi:10.1017/aog.2016.15.

Woodhead JD, Hergt JM (2000). Pb-Isotope Analyses of USGS Reference Materials. *Geostandards Newsletter* 24(1): 33–38. doi:10.1111/j.1751-908x.2000.tb00584.x.

Yanai K (1991). Gabbroic meteorite Asuka-31: Preliminary examination of a new type of lunar meteorite in the Japanese collection of Antarctic meteorites. *Lunar and Planetary Science Conference Proceedings* 21: 317–324. bibcode:1991LPSC...21..317Y.

Yanai K, Kojima H (1991). Varieties of lunar meteorites recovered from Antarctica. *Antarctic Meteorite Research* 4: 70–90. bibcode:1991AMR.....4...70Y.

Zeigler RA, Korotev RL, Jolliff BL, Haskin LA (2005). Petrography and geochemistry of the LaPaz Icefield basaltic lunar meteorite and source crater pairing with Northwest Africa 032. *Meteoritics & Planetary Science* 40(7): 1073–1101. doi:10.1111/j.1945-5100.2005.tb00174.x.

Zhang A, Hsu W, Li Q, Liu Y, Jiang Y, Tang G (2010). SIMS Pb/Pb dating of Zr-rich minerals in lunar meteorites Miller Range 05035 and LaPaz Icefield 02224: Implications for the petrogenesis of mare basalt. *Science China Earth Sciences* 53(3): 327–334. doi:10.1007/s11430-010-0041-z.

Zwally HJ, Giovinetto MB, Beckley MA, Saba JL (2012). Antarctic and Greenland Drainage Systems.